Doctoral Thesis

Robust assessment of quantitative magnetic resonance imaging as an imaging biomarker at 7 Tesla

Dongkyu Lee

Department of Biomedical Engineering

Graduate School of UNIST

2020

Robust assessment of quantitative magnetic resonance imaging as an imaging biomarker at 7 Tesla

Dongkyu Lee

Department of Biomedical Engineering

Graduate School of UNIST

Robust assessment of quantitative magnetic resonance imaging as an imaging biomarker at 7 Tesla

A thesis/dissertation
submitted to the Graduate School of UNIST
in partial fulfillment of the
requirements for the degree of
Doctor of Philosophy

Dongkyu Lee

8. 20. 2019 of submission
Approved by

_____

Advisor
HyungJoon Cho

Robust assessment of quantitative magnetic resonance imaging as an imaging biomarker at 7 Tesla

Dongkyu Lee

This certifies that the thesis/dissertation of Dongkyu Lee is approved.

08. 20. 2019

_____

Advisor: HyungJoon Cho

_____

Woonggyu Jung

_____

Joon-Mo Yang

_____

Jung-Hoon Park

_____

Sohyun Han

Abstract

Magnetic susceptibility contrast MRI using local magnetic field gradients or inhomogeneities is expected to provide low-resolution quantification of tissue microarchitecture, as magnetic resonance (MR) transverse relaxation times (T_2 and T_2^*) are influenced by field inhomogeneity arising from susceptibility mismatch of tissues. By aid of ultra-high field MRI scanner, MR transverse relaxation times is promising to further increase their sensitivity to detecting subtle structural changes in tissue microstructures. However, one of the main technical difficulty of ultra-high field MRI is unwanted variations of signal and contrast, or even worse, nullify the MR signal due to increased macroscopic static magnetic field inhomogeneities which are prone to misinterpretation and loss of structural information. This study focuses on improving the sensitivity and the robustness of ultra-high field MRI (particularly for 7 T) from unwanted signal variations due to magnetic field inhomogeneities and shortened MR transverse relaxation times. MR transverse relaxation times were investigated for the low-resolution assessment of tissue microstructures, such as trabecular bone microstructure and cerebral microvasculature. As a result, T_2 relaxation time without having an effect of macroscopic field inhomogeneities may be suitable for the assessment of trabecular structural indices and robust with degrading spatial resolution with reduced scan time at 7 T. For the assessment of cerebral microvasculature, the diffusion-time-dependent stimulated-echo-based MR relaxation-rates was demonstrated as robust measures for assessing small (diameter < 5 μm) cerebral microvasculature, where macroscopic field inhomogeneities from bone (air)-tissue interfaces and influences of large vessels in cortical region are significant. Finally, the quantification of MR longitudinal relaxation time (T_1) was optimized by variable repetition-delay turbo-spin echo method with sparse encoding technique.

Keywords: magnetic resonance relaxations, magnetic resonance spatial resolution, trabecular structure, vessel size imaging (VSI), stimulated echo (STE), compressed sensing, T_1 measurements, turbo-spin echo (TSE), rapid acquisition with refocused echoes (RARE).

Contents

List of figures

List of tables

Abbreviations

ADC	Apparent diffusion coefficient
BVF	Bone volume fraction
BVf	Blood volume fraction
CCC	Concordance correlation coefficient
CS	Compressed sensing
CS-TSE	Compressed sensing assisted turbo spin echo
CT	Computed tomography
FID	Free induction decay
FOV	Field of view
D	Diffusion coefficient
Gd-DOTA	Gadolinium-DOTA
IRSE	Inversion recovery spin echo
KESM	Knife-edge scanning microscope
mVD	Mean vessel diameter
MC	Monte Carlo
MEGE	Multi echo gradient echo
MGE	Multi gradient echo
MR	Magnetic resonance
MRI	Magnetic resonance imaging
MSME	Multi slice multi echo
NC	Neocortex
OB	Olfactory bulb
RF	Radio frequency
ROI	Region of interest
SE	Spin echo
SNR	Signal to noise ratio
SPION	Superparamagnetic iron oxide nanoparticles
STE	Stimulated echo
T	Tesla
TD	Diffusion duration
TF	Turbo factor
Tb.Sp	Trabecular spacing
Tb.N	Trabecular number

Tb.Th	Trabecular thickness
TE	Echo time
TR	Repetition time
TrueFISP	True fast imaging with steady-state precession
TSE	Turbo spin echo
UTE	Ultra short echo time
VSI	Vessel size index
WM	White matter
1D	One dimensional
2D	Two dimensional
3D	Three dimensional

1. Introduction

Magnetic resonance imaging (MRI) noninvasively provides in vivo imaging method without ionizing radiation unlike computed tomography or positron emission tomography. MRI can be performed by various acquisition methods called pulse sequences, which provides boundless image contrasts for soft tissue as well as calcified tissue. In recent years, MRI has improved dramatically in both signal- and contrast-to-noise ratio through ultra-high field (above 7.0 T of the static magnetic field B_0) MRI scanner. Ultra-high field MRI makes possible sub-millimeter isotropic imaging, which is challenging on a conventional high-field (1.0 T to 3.0 T) scanner. In addition, it also provides new contrast mechanisms which has been limited due to its insufficient sensitivity at lower fields.

Magnetic susceptibility (χ) contrast MRI using local B_0 field gradients or inhomogeneities (ΔB_0) is expected to provide low-resolution quantification of tissue microarchitecture, as magnetic resonance (MR) transverse relaxation times (T_2 and T_2^*) are influenced by ΔB_0 arising from susceptibility mismatch of tissues ($\Delta\chi$). Previous researches demonstrated considerable but changing relationships between measured T_2 and T_2^* values with tissue micro-structures. With the recent advance of ultra-high field MRI, the increasing T_2 and T_2^* contrasts support to enhance their sensitivity to a subtle structural changes of tissue microstructures.

One of the main technical difficulty of ultra-high field MRI is the severe macroscopic ΔB_0 near the boundary of the tissues with large $\Delta\chi$. This increased macroscopic ΔB_0 of ultra-high field MRI leads to unwanted variations of signal and contrast, or even worse, void of signal which are prone to misinterpretation and loss of structural information. Reducing voxel size (or increasing spatial resolution) is commonly employed to avoid these signal variations by minimizing ΔB_0 within the imaging voxels. However, increasing required resolution of MRI directly elongates to the total scan time which limits feasibility and potential clinical advantages, and causes additional burdens in the post-image processing and reproducibility due to motional degradation. Along with the macroscopic ΔB_0, shortened T_2 and T_2^* values at above 7 T often limits the applicability of fast multi-echo methods due to signal distortion and broad point spread function.

1.1 Thesis outline

In Chapter 2, the basic background of MR imaging is briefly introduced for the aspect of signal and contrast generations.

For the first subject of the study (Chapter 3 and Chapter 4), magnetic susceptibility contrast was investigated for the low-resolution quantification of tissue microstructures, such as trabecular bone microstructures and cerebral microvasculature.

In the second subject (Chapter 5), the multi-slice mapping of the MR longitudinal relaxation time (T_1) was optimized by multiple repetition-time turbo-spin-echo method with an assist from compressed-sensing sparse encoding technique.

2. Background

2.1 Signal generation and spatial encoding

Generally, the MRI signal is normally obtained from the water molecules in the human tissues, primarily coming from protons. When a patient located in the MRI scanner, protons precesses along with a static main magnetic field (B_0), which consequently yield a net magnetic moment or magnetization (M_0) oriented to B_0 direction (longitudinal direction). The precession frequency of the protons in a constant B_0 is calculated from the Larmor Equation:

$$\omega_0 = \gamma B_0 \quad [2.1]$$

where ω_0 represents the Larmor frequency and γ is the gyromagnetic ratio for protons (42.57 MHz/T). After applying a sequence of radiofrequency (RF) pulses with the Larmor frequency, the longitudinal magnetization (M_z) is manipulated and produces the MR signal by rotating the magnetization into transverse plane, which called RF excitation. This resulting magnetization in the transverse plane (M_{xy}) induces a voltage change in a receiver coil set to the corresponding Larmor frequency. The received MR signal is the vector sum of all the RF excited transverse magnetization in the imaging region. With a uniform or homogeneous B_0 in the tissue of interest, the MR signal has a single sharp peak at the Larmor frequency. The spatial information of the magnetization can be encoded by applying spatially varying gradient fields ($G(r)$, at the position r) using additional coils which create a spatial distribution in the precession frequency of the magnetization:

$$B(r) = B_0 + G(r) \quad [2.2]$$

$$\omega(r) = \gamma B(r) = \gamma B_0 + \gamma G(r) = \omega_0 + \gamma G(r) \quad [2.3]$$

and the corresponding spatially encoded transverse magnetization is

$$M_{xy}(r,t) = \rho(r) \cdot exp(-i\omega(r)t) = \rho(r) \cdot exp(-i(\omega_0 + \gamma G(r))t) \quad [2.4]$$

where $\rho(r)$ is the proton density. The phase gain (or accumulation) due to the linear gradient field during a time t at the position r is

$$\phi(r,t) = \gamma G(r)t = 2\pi k_r(\mathrm{t})\mathrm{r} \quad [2.5]$$

$$M_{xy}(r,t) = \rho(r) \cdot exp(-i2\pi k_r(\mathrm{t})\mathrm{r}) \quad [2.6]$$

where the spatial frequency $k_r(t)$ is the phase cycles per unit distance along *r*-direction. For any arbitrary gradient shape and direction *r*

$$k_r(\mathrm{t}) = \frac{\gamma}{2\pi}\int_0^t G(r,t)dt \quad [2.7]$$

The signal from an excitation with a gradient field can be represented as

$$S(k) = \int M_{xy}(r,t)dr = \int \rho(r) \cdot exp(-i2\pi k_r(t)r)\, dr \quad [2.8]$$

The spatial information of the proton density can be evaluated by utilizing the Fourier transform for this spatially encoded MR signal in the *k*-domain (*k*-space).

$$\rho(r) = \int S(k) \cdot exp(i2\pi k_r(t)r)\, dk \quad [2.9]$$

The point spread function of the MR signal affected by B_0 inhomogeneities and the proton interactions with their environment which modulate the precession frequency.

2.2 Longitudinal and transverse relaxation times

After RF excitation (at time t = 0), the magnetization tends to return to their equilibrium distribution (the thermal-equilibrium state) by interaction and processes with the local environment. The longitudinal magnetization (M_Z) returns toward equilibrium (to its maximum value) with a characteristic time constant T_1.

$$M_z(t) = M_0\left(1 - \exp\left(-\frac{t}{T_1}\right)\right) + M_z(0)\exp\left(-\frac{t}{T_1}\right) \quad [2.10]$$

The mechanisms of T_1 relaxation are related with the fluctuation of local B_0 at the Larmor frequency as a result of the molecular rotation and translation via dipole-dipole interactions. The T_1 relaxation rate relates to the mobility, coupling, and macromolecular binding of the molecules.

The decays of transverse magnetization are characterized by characteristic time constants (T_2 and T_2^* relaxation times).

$$M_{xy}(t) = M_{xy}(0)\exp\left(-\frac{t}{(T_2 \text{ or } T_2^*)}\right) \quad [2.11]$$

The T_2 relaxation caused by random dipole-dipole interactions with neighboring spins which change local magnetic field and disperse the precession frequency. This causes dephasing and eventually M_{xy} decays back to zero (when losing phase coherence completely). T_2^* relaxation includes both the T_2 relaxation and dephasing due to B_0 field inhomogeneities (T_2').

$$\frac{1}{T_2^*} = \frac{1}{T_2} + \frac{1}{T_2'} \quad [2.12]$$

The time constants of these MR relaxations are used in MRI as a origin of contrast.

2.3 Magnetic susceptibility

The magnetic susceptibility χ, a dimensionless constant, indicates how easily a sample becomes magnetized in reaction to the applied B_0 field. The effective local magnetic field led by a magnetic susceptibility is characterized as following:

$$B_{eff} = (1 + \chi)B_0 \quad [2.13]$$

The bulk susceptibility of tissue is diamagnetic ($\chi < 0$), whereas the nuclear susceptibility of a proton is paramagnetic ($\chi > 0$). The magnetic susceptibility induced local B_0 shift give image contrasts and may cause artifacts in the acquired images.

3. The robust assessment of trabecular bone structural index using T_2 value with multiple acquisition resolutions at 7 T

3.1 Introduction

Measuring the resistance to fracture of a bone via bone mineral density from dual-energy x-ray absorptiometry has been employed clinically to evaluate the overall bone strength [1-3]. However, multiple previous findings show that trabecular micro-structural indices, such as trabecular spacing (Tb.Sp), trabecular number (Tb.N), trabecular thickness (Tb.Th), and bone volume fraction (BVF), also takes an important role to decide an entire strength of a bone, diagnose bone fracture risks, and monitor a treatment response [4-6]. However, resolving 3D micro-architectural information of a trabecular bone via high-resolution micro-CT imaging may be restricted by elevated radiation doses because, normally, the thickness of a human trabeculae is in the range from 100 to 150 mm together with complicated microscopic structural variations [7,8].

The micro-MRI for spatial resolution under 250 mm^2 with slice-thickness of approximately 1.5 mm ensures quantifications of trabecular micro-structures within 15-minute without radiation exposure [9]. However, unwanted patients motion during lengthy scan duration and the necessary SNR may hinder the application of a micro-MRI largely due to the both required subsequent image processing and fidelity [10]. Moreover, the accuracy for the evaluation of micro-structural indices rapidly decreases with worsening the MR acquisition resolution, as reported in the previous studies [11-13].

It is widely known that the MR transverse relaxation times (T_2 and T_2^*) are largely contributed by a tissue micro-architecture. Thus, measurement of T_2 and T_2^* can be utilize for the low-resolution quantification of trabecular micro-structural indices, as MR transverse relaxation are largely affected by local B_0 inhomogeneities rooted in mismatch of the magnetic susceptibilities between of trabecular bones and nearby marrows [14-21]. Thus, the results of previous studies state considerable, but vacillating correlations (primarily for T_2^*) with certain tissue microstructural parameters [22-27]. For this reason, the advisory representations are required to directly link absolute T_2^* relaxation times with the micro-structural index because the results may depend on the MR experimental parameters, such as the imaging voxel size [18,28,29].

With a recent advance in increasing magnetic field strength of MRI, the enhanced MR transverse relaxations are expected to further sensitive to the subtle changes in a trabecular micro-structure. Thus, MR relaxometry may promote the low-resolution estimations of a bone strength. Previous research demonstrated the reachability of measuring short T_2^* values of trabeculae (< 10 ms) by employing UTE-MRI even at high field, and the link between T_2^* with micro-structural information of trabeculae

have been studied at various static B_0 strengths [27]. However, to maintain a meaningful correlation with trabecular microstructural indices, the T_2^* relaxation values required to be stable especially with a low acquisition resolution because the MR acquisition resolution largely contributes to the T_2^* relaxation based on the static dephasing. On the contrary, the diffusing protons located in the strong magnetic field gradients near surface of trabecular bone are mainly responsible for the T_2 relaxation. Therefore, even for the same condition, the MR acquisition resolution may result in different effects on the transverse relaxations between spin-echo and gradient-echo methods. However, the influence of MR imaging voxel size on T_2 and T_2^* relaxations have not been studied in a systematic way, especially for trabecular bone at the high static field strength of 7 T, while acquiring MR transverse relaxation times of trabeculae at low-acquisition resolutions may take the direct advantage of shortened total scan duration against high-resolution micro-MRI [30].

First, the dependency of MR imaging voxel sizes on the both T_2 and T_2^* relaxations were explored through a Monte-Carlo (MC) simulations for molecular diffusion under local B_0 inhomogeneities from trabecular bones and bone marrows [31]. Second, MR transverse relaxations were systemically compared with reference trabecular micro-architectural parameters from micro-CT images, which considered as a gold standard method, by means of ex vivo defatted human trabecular experiments with degrading MR acquisition resolutions on a preclinical 7 T scanner. Third, the consistency of MR transverse relaxation times for bone marrow containing bovine knee trabecular samples (n = 4) were examined with varying MR acquisition resolutions on a clinical 7 T MRI.

3.2 Methods

MC simulations for the MR transverse relaxations of trabeculae

MC proton diffusion simulations were conducted to demonstrate the influences of the MR imaging voxel size to the transverse relaxations with a trabecular bone from a micro-CT image. The MC simulation was computed on the MATLAB (MathWorks, Natick, MA, R2016b environment) with reference to the finite perturber method [32] and as employed for the previous studies [33,34]. The variations in the local magnetic field (ΔB) from the magnetic susceptibility difference between trabecular bone and nearby marrow was evaluated by computing the convolution of each B_0 shift occurred from the finite perturbers in trabeculae. The magnetic susceptibilities for the bone marrow (water) and trabeculae were used at −12.96 ppm and −38.40 ppm, respectively (CGS unit, estimated from the magnetic susceptibility of calcium carbonate) [35]. The anatomies for the simulation volumes were determined with forty bone images ($992 \times 992 \times 992$ mm^3) from 3D micro-CT images of defatted samples (Figure 3.1A). The volumes were rescaled to the isotropic voxel size at 1 mm^3 by performing cubic-spline interpolation as shown in Figure 3.1B. The ΔB maps for the simulation

volumes were computed from the finite perturber method. Moreover, in order to minimize periodic boundary effects caused by using the Fourier transform convolution, the center regions of computed ΔB maps (500 × 500 × 500 mm^3 for each simulation volume) were employed for the further processes (Figure 3.1C and 3.1D). The unit grid size and the unit time (Δt) for the simulation were 1 mm^3 and 10 ms, respectively. At the beginning, 125,000,000 (500 × 500 × 500) diffusion protons were evenly spread over the simulation volume (1 proton per each grid). Protons located in the bone region were discarded in order to prevent the MR signal from the bone region. MC method was applied together with a periodic boundary at the edges of the simulation volume. The diffusion length for each simulation step was set to $\sqrt{2D\Delta t}$, where D denotes the diffusion coefficient of free water of 2300 mm^2s^{-1}. The accumulated phase of the diffusing protons over diffusion duration was computed. Accordingly, by taking the mean phase factor for the total protons in the voxel of interest, the MR signal of the trabecular bone sample was evaluated at multiple voxel sizes of 125, 250, and 500 mm^3 which corresponding to the resolutions for the ex vivo experiments.

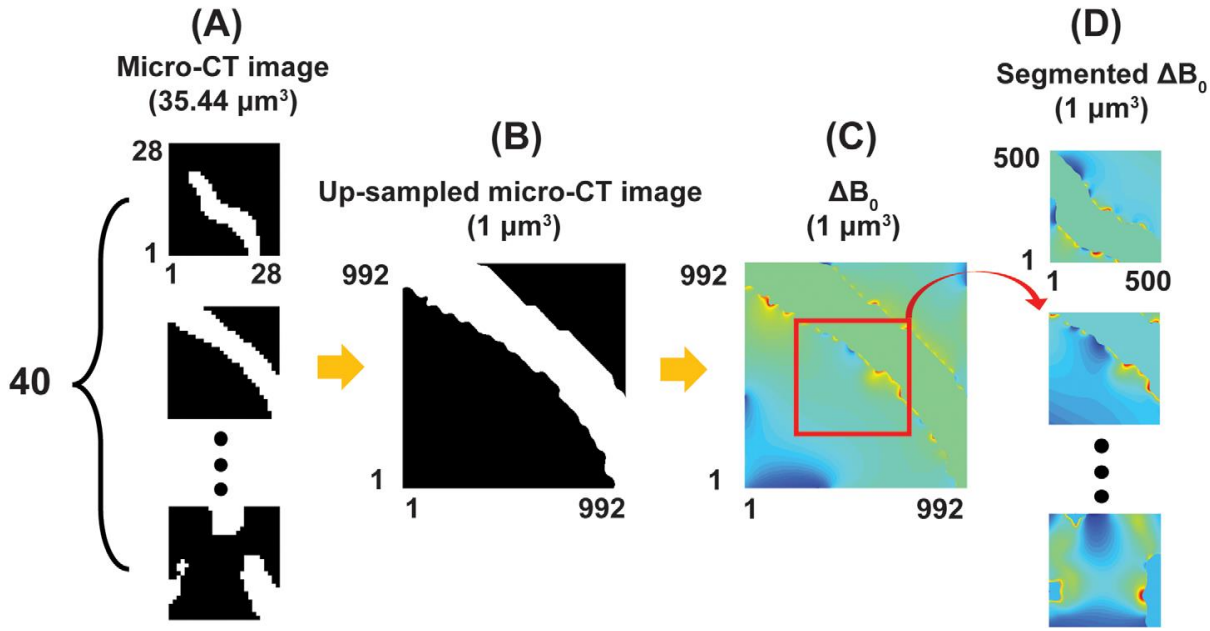

Figure 3.1 The illustration for the steps to calculate B_0 shift from bone. Trabecular bone images from a micro-CT acquisition were divided into 40 sub-volumes (A) and rescaled according to the simulation unit grid (B). Calculated ΔB_0 from the finite perturber method (C). In order to minimize the unwanted values from the fast Fourier transform convolution, the outer volume of the resulting ΔB_0 was removed (D).

The MR signal for UTE and multi-slice multi-echo (MSME) methods were computed using most of MR parameters utilized for the ex vivo defatted human trabecular experiments (Table 3.1). The input

parameters were slightly modified as follows: TEs of the UTE were 10, 50, 100, 500, and 1000 ms, and TE for the MSME was ranging from 4 to 40 ms with evenly displaced echo-spacing of 4 ms. Corresponding MR signals for the imaging volume sizes of 125, 250, and 500 mm^3 were calculated. Voxel-wise T_2 and T_2^* values for each volume were evaluated from the following mono-exponential decay equation:

$$S(t) = S_0 \times exp\,(-TE/(T_2^*\ or\ T_2)) \quad [3.1]$$

A nonlinear least-squares-fitting script on the MATLAB environment was used for the T_2 and T_2^* calculation.

Table 3.1 The MR acquisition parameters for ex vivo experiments. Defatted human trabecular and bovine knee experiments for measuring MR transverse relaxation times were performed on a preclinical and a clinical 7 T systems, respectively.

	Pulse sequences	Excitation flip angle [°]	Refocusing flip angle [°]	TR [ms]	TE [ms]	Field of view [mm^3]	Voxel size [μm^3]	Receiver bandwidth [Hz/voxel]	Number of scans	Scan time [min]
Defatted human trabecular experiment	UTE	15		70	0.008, 0.05, 0.1, 0.5, 1, 10, and 50	16 × 16 × 16	125 × 125 × 125 250 × 250 × 250 500 × 500 × 500	2343.75	1	420 104 26
	MSME	90	180	1000	Approx. 5-320 (echo spacing = 5)	16 × 16 × 16	125 × 125 × 125 250 × 250 × 250 500 × 500 × 500	3125	1	273 68 17
Ex vivo bovine knee experiment	MEGE	15		100	Approx. 2.8-16.8 (echo spacing = 2.4)	60 × 68 × 12	400 × 400 × 500 600 × 600 × 750 800 × 800 × 1000 1000 × 1000 × 1250	auto adjust	1	8.5 4 2 1.5
	MSME	90	180	500	Approx. 8.5-144.5 (echo spacing = 17)	60 × 68 × 12	400 × 400 × 500 600 × 600 × 750 800 × 800 × 1000 1000 × 1000 ×1250	auto adjust	1	11 5 3 2
	TSE	90	180	500	11 (turbo factor = 4)	60 × 68 × 12	200 × 200 × 250	auto adjust	1	22.5

Defatted human trabecular bone experiment

This study was approved by the Ulsan National Institute of Science and Technology institutional review board in agreement with the guidelines of the Helsinki Declaration. Four human trabeculae were sampled from the distal femoral condyle during knee joint replacement operation. The trabecular samples were cut into 1 × 1 × 1 cm^3 size. The marrow was eliminated by using a Soxhlet apparatus with a mixed solvent (110 ℃) of chloroform/methanol (2:1, v/v) for 24 hours [36]. Each defatted trabecular specimen was move into a 10% solution of an enzyme-active powdered detergent with distilled water and washed alternately with ultrasonication for 10 hours. For the MRI and micro-CT experiments, each cubic trabecular was soaked in a water chamber filled with distilled water, degassed, and takes place into a syringe with distilled water. High-resolution anatomical images from micro-CT and UTE-MRI acquisitions were utilized to examine air bubbles in the samples.

T_2 and T_2^* values (3D MSME and 3D UTE pulse sequences, respectively) for the bone-marrow removed specimens were evaluated with multiple imaging voxel sizes of 125, 250, and 500 mm^3. The ex vivo experiment was conducted by using a 25-mm transceiver RF coil on a Bruker's 7 T system

(Billerica, MA). The MRI experimental parameters of the ex vivo experiments are described in Table 3.1.

3D high-resolution micro-CT experiment were conducted to obtain the reference trabecular structural information on a Bruker SkyScan 1176 system. The trabecular samples were placed on the bed and fixed to avoid mechanical vibration during the scan. Micro-CT imaging were conducted as follows: exposure time of 100 ms, source voltage of 90 kV, source current of 259 μA, isotropic acquisitio006E resolution of 35 mm^3, 0.11 mm thick copper filter, 360 ° rotation scanning (rotation step of 0.7 °), and three frame average. A NRecon image reconstruction software (Bruker) was utilized with a beam hardening correction of 98 % and ring artifact correction of 6.

Binary bone regions from the UTE and the micro-CT were extracted by performing the image segmentation [37], and corresponding micro-CT images were matched to the MRI images by using a 3D rigid body registration. The micro-structural parameters from the micro-CT and the UTE images were calculated with a 3D sphere fitting method [38,39] in BoneJ software [40].

The voxel based T_2 and T_2^* values for the defatted trabecular specimens were calculated using the Eq. 3.1. For minimizing the difference in the intrinsic T_2 values of the solutions (can be changed by the temperature and shimming), each T_2 and T_2^* value of the samples was rescaled by compensating the T_2 in the water-only region of the samples.

$$\text{normalized } T_2 \text{ or } T_2^* = \frac{T_2 \text{ or } T_2^*}{\text{mean } T_2 \text{ of water only region}} \quad [3.2]$$

Before calculating the correlations, sub-regional mean values of each parameter map were evaluated. To be specific, trabecular bone included regions (9.375 × 9.375 × 9.375 mm^3) of each specimen were sectioned and separated into 27 (3 × 3 × 3) sub-volumes. The number of the sub-volumes for each parameter map was 108 (27 × 4 bone samples with a volume of 3.125 × 3.125 × 3.125 mm^3). The rationale for the sub-regional analysis has been demonstrated in the previous studies [41-43]. The results of the study verified that the local changes in trabecular micro-structure can be exist even for healthy subjects [44]. Thus, sub-regional approach with 3 mm^3 volume was employed, which approximately six-times the lowest MR resolution together with an enough dynamic value range of each parameter map. The sub-regional mean value of each parameter map was utilized for the further analysis. Accordingly, the correlation coefficients for each MR trabecular parameter map were calculated with respect to the reference micro-CT trabecular structural index maps at the multiple MRI voxel sizes.

Ex vivo bovine bone experiment

Bovine knee articular cartilages (n = 4) were purchased at a local butcher. Each bovine bone was trimmed to fit in a 16-channel wrist array-coil receiver (RAPID Biomedical GmbH, Rimpar,

Germany), and ex vivo experiments for the bovine bones were conducted on a Philips Achieva 7 T MRI scanner (Philips Healthcare, Cleveland, OH, USA). 3D MR transverse relaxation times were mapped for multi-echo gradient-echo (MEGE) and MSME methods (T_2^* and T_2 relaxation times, respectively) at the voxel sizes of 0.4 × 0.4 × 0.5, 0.6 × 0.6 × 0.75, 0.8 × 0.8 × 1, and 1 × 1 × 1.25 mm^3. The 3D high-resolution (0.2 × 0.2 × 0.25 mm^3) turbo-spin-echo (TSE) image was obtained to evaluate trabecular micro-architectural indices. To minimize the image aliasing along slice-direction, phase encoding along the Z-direction was oversampled by 150% for each MRI acquisition. The detailed acquisition parameters for the ex vivo bovine bone experiment are shown in Table 3.1. MR transverse relaxation values were calculated by Eq. 3.1. Corresponding structural indices were evaluated for the high-resolution TSE acquisition. Sub-regional analysis was applied with each sub-region volume of 6 × 6 × 6 mm^3 and corresponding correlations were evaluated.

3.3 Results

MC Simulations

The dependency of MR transverse relaxations on both TE and spatial resolution is described in Figure 3.2. At the TE of 0 ms, spins were evenly distributed in the water or bone marrow region with no accumulated phases, and the spin density with zero value in the top row is the trabecular bone area. The phase of diffusing protons was accumulated with increasing TE as a result of ΔB_0 and diffusion (second row of Figure 3.2A and Figure 3.2B). This dephasing of the spins within the voxels decreases the corresponding MRI signal because the MRI signal is obtained by averaging the total phases in the voxel of interest. Thus, MR T_2 and T_2^* relaxation time from gradient- and spin-echoes, respectively, can be acquired by monitoring the MR signal decaying along with the TE. The signal decaying for the gradient-echo based UTE acquisition observed faster at larger the imaging voxel size, which explains overall shortening of T_2^* relaxation times of the UTE with degrading spatial resolutions.

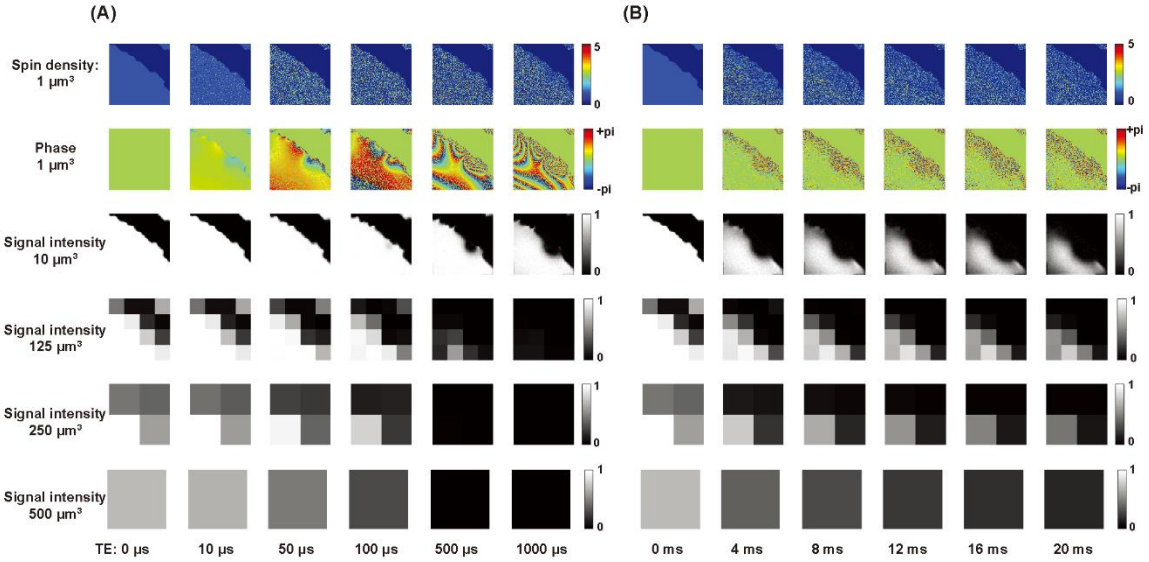

Figure 3.2 Simulated MRI phases and signal intensities for UTE and MSME acquisitions at multiple imaging voxel sizes. The accumulated phases and corresponding TE images at various sizes of image voxels for UTE (A) and MSME (B) acquisition along with TEs.

Figure 3.3A and 3.3B compare the distribution of simulated and experimentally acquired T_2 and T_2^* values at various sizes of MR imaging voxels. The ratio of T_2 /T_2^* was an order of 10^2 for both simulation and experiment. The T_2 and T_2^* values for the simulation were normalized to the experimental values for the direct comparison of the distribution. The dynamic range for T_2^* distribution was reduced as degraded the spatial resolution for both the simulation and experiment. Contrary, the dynamic range of the T_2 distribution for both simulation and experiment were free to the MR acquisition resolution.

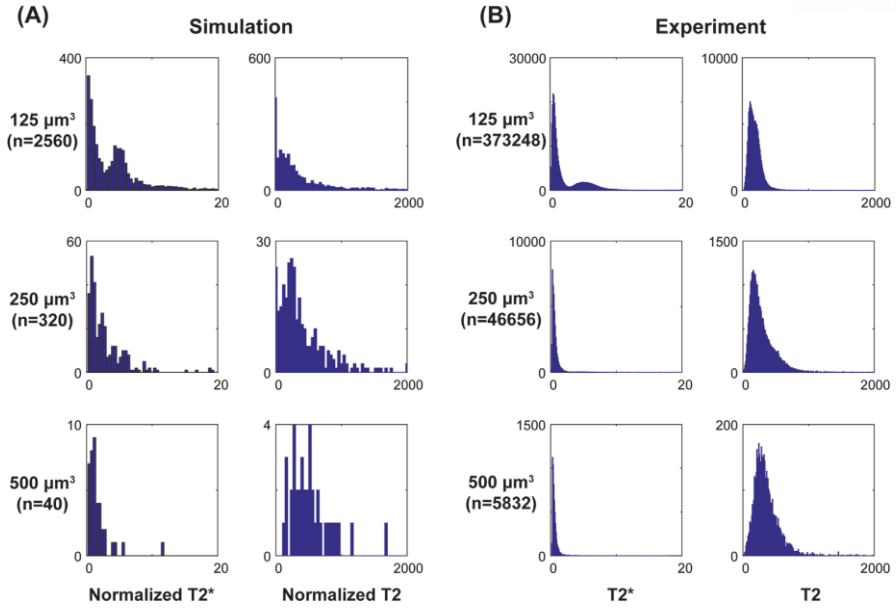

Figure 3.3 Histograms of the simulated (A) and experimentally acquired (B) T_2 and T_2^* relaxation times.

Ex vivo defatted human trabecular experiment

Representative binary bone images for UTE and micro-CT methods were illustrated in Figure 3.4A. Each high-resolution micro-CT bone image was matched to the rescaled UTE bone image by employing a rigid-body registration (Figure 3.4B). Figure 3.4C presents the volume rendered trabecular bone images after the registration process.

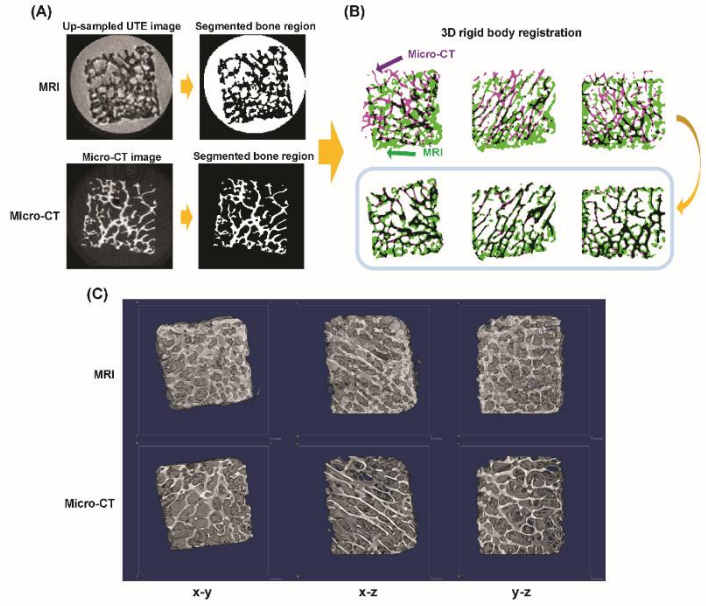

Figure 3.4 Image registration for MRI and micro-CT trabecular bone images. (A) Up-scaled UTE-MRI, and micro-CT images (35 μm^3), and corresponding segmented bone images. (B) Segmented binary bone images for before and after 3D rigid body registration. (C) Volume rendered bone images

after the image registration.

Figure 3.5 illustrates the sub-regional analysis procedures to compare the MRI transverse relaxation time and trabecular parameters with respect to the micro-CT trabecular structural indices.

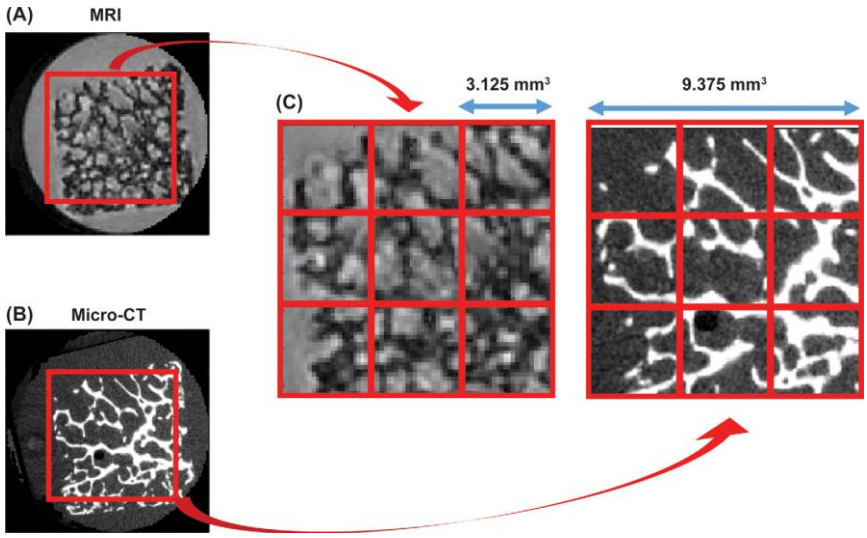

Figure 3.5 Conceptual illustrations of sub-regional analysis for the correlations between MRI (A) and micro-CT (B). Regional mean value for each subregion (volume of 3.125 mm^3) were utilized for the correlations of MRI and micro-CT trabecular indices.

The sub-regional mean values of each trabecular bone parameter were utilized to evaluate the correlations of MRI and micro-CT. The correlations for the UTE and the MSME methods were calculated with respect to the reference micro-CT trabecular structural indices at various imaging resolutions. Consistent correlations were obtained for both UTE ($r_{Tb.Sp} = 0.802^{***}$, $r_{Tb.N} = 0.666^{***}$, $r_{Tb.Th} = 0.534^{*}$, and $r_{BVF} = 0.779^{***}$) and MSME ($r_{Tb.Sp} = 0.704^{***}$, $r_{Tb.N} = 0.583^{***}$, $r_{Tb.Th} = 0.234^{*}$, and $r_{BVF} = 0.493^{***}$) for the high-resolution of 125 μm^3. For both UTE and MSME, the correlations quickly degraded with increasing the size of imaging voxel. This is primarily because of the larger MRI voxel size than the typical trabecular thickness of 100 to 200 μm, which results in the inappropriate bone region segmentation. The highest correlation for the MRI structural indices was acquired for Tb.Sp which illustrated in Figure 3.6.

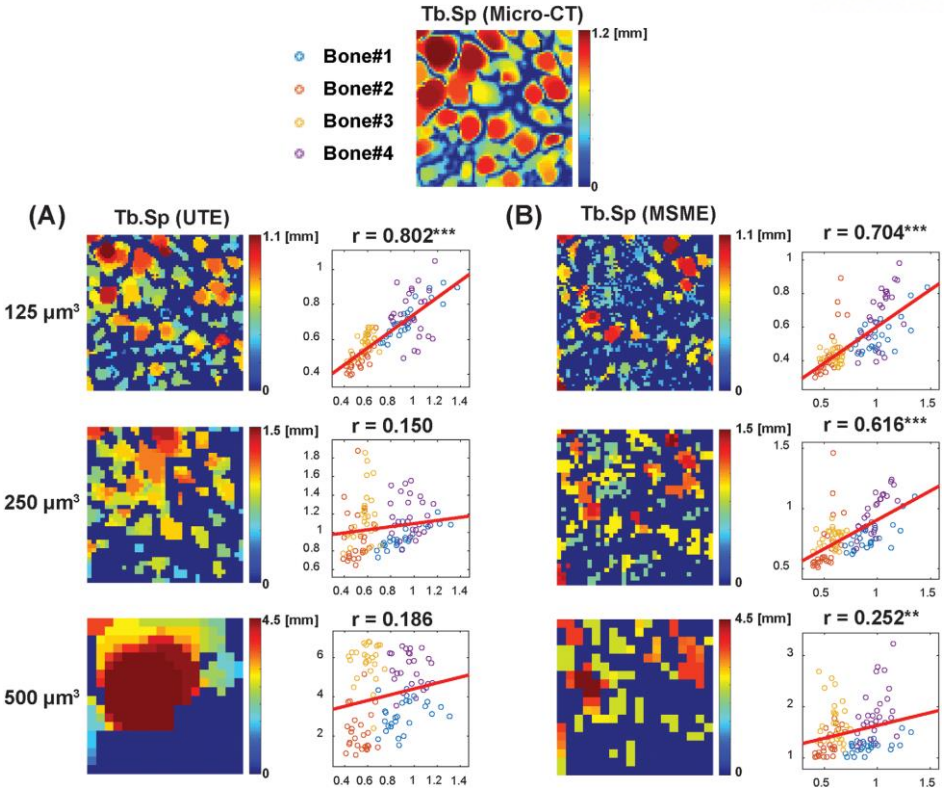

Figure 3.6 Correlation analysis of Tb.Sp from MRI and micro-CT acquisitions with four defatted human trabecular bone specimens. Tb.Sp calculated from UTE (A) and MSME (B) were shown at multiple acquisition resolutions of 120, 250, and 500 mm^3. In the scatter plots, the sub-regional mean value for each specimen was color-coded.

Figure 3.7 presents the resulting correlations for T_2 and T_2^* with respect to micro-CT Tb.Sp. Significant correlations of both T_2 and T_2^* values were observed with regard to micro-CT Tb.Sp and Tb.N at high-resolution of 125 mm^3 ($r_{\text{Tb.Sp and } T_2^*} = 0.841^{***}$, $r_{\text{Tb.N and } T_2^*} = -0.789^{***}$, $r_{\text{Tb.Sp and } T_2} = 0.878^{***}$, and $r_{\text{Tb.N and } T_2} = -0.878^{***}$). The correlation between T_2^* and Tb.Sp was steadily degraded as increasing MR acquisition resolution (Figure 3.7A), while the correlation for T_2 was preserved strongly even at the low-resolutions (Figure 3.7B).

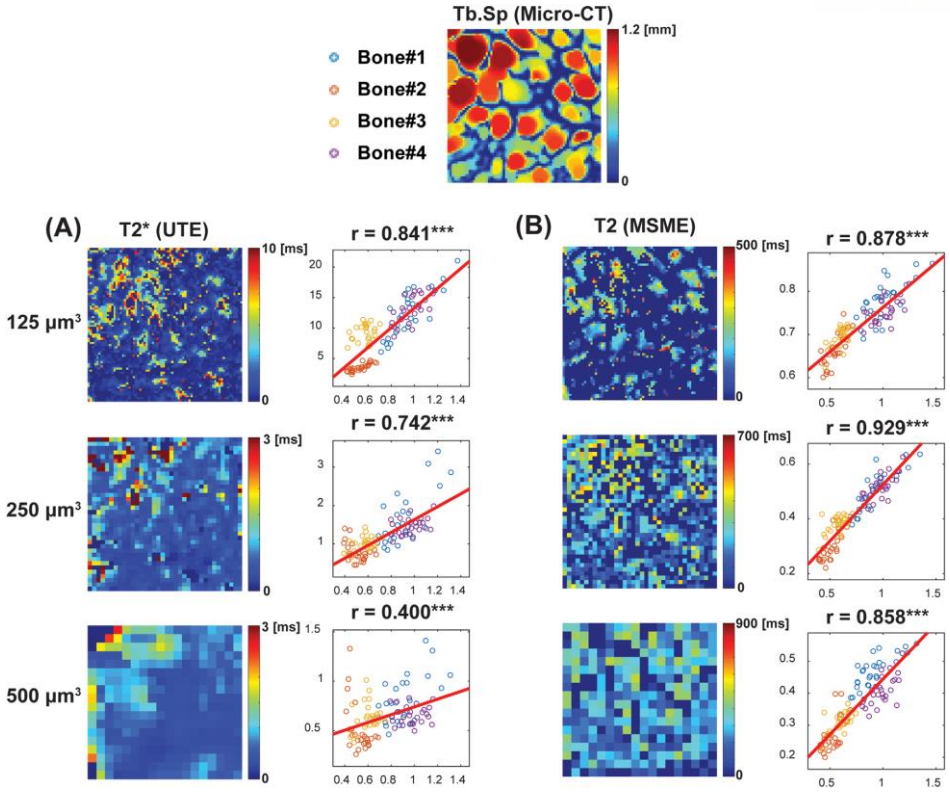

Figure 3.7 Correlation analysis of Tb.Sp between MRI T_2 and T_2^* values for four defatted trabecular bone samples. The correlation between reference micro-CT Tb.Sp with T_2^* (A) and T_2 (B) relaxation times for the MRI resolutions of 120, 250, and 500 mm^3. In the scatter plots, the sub-regional mean value for each specimen was color-coded.

Figure 3.8 shows the relation between the MR acquisition resolution with the correlation coefficients for the defatted trabecular experiments. For the MRI Tb.Sp and Tb.N at the high-resolution of 125 mm^3, structural parameters from the UTE provided stronger correlation coefficient with respect to micro-CT than MSME probably due to a reduced TE for UTE. Although the correlations were weak for the Tb.Th and BVF, UTE was also superior to MSME. The correlations of structural indices for both from UTE and MSME acquisitions degraded significantly at acquisition voxel size over 250 mm^3, which is in accordance with the MC simulation results and previously reported study [11].

Both T_2 and T_2^* relaxation times were significantly related to the reference micro-CT Tb.Sp and Tb.N at a high-resolution of 125 mm^3. As increasing MRI voxel size, the correlation coefficients for MR transverse relaxation times with reference to micro-CT Tb.Sp and Tb.N were kept solely with T_2 relaxation time, while those for T_2^* dropped dramatically with decreasing absolute T_2^* values and shrinking dynamic range.

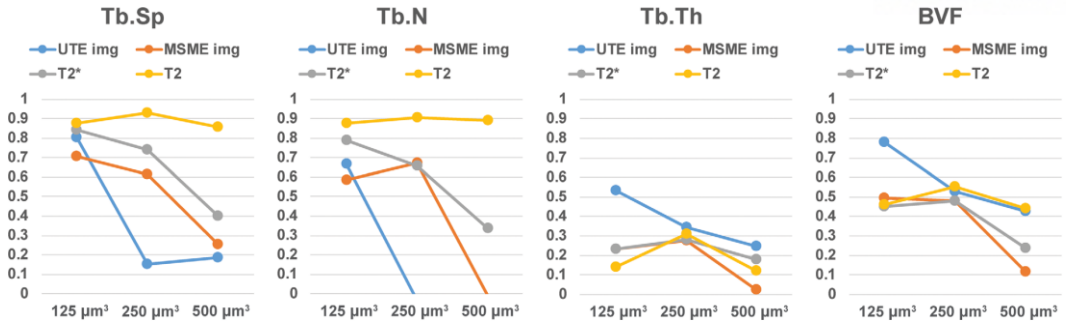

Figure 3.8 MR sensitivities and resolution dependency to trabecular structural indices. The correlations for MRI trabecular structural indices and relaxation times were evaluated with respect to reference micro-CT trabecular structural indices, such as Tb.Sp, Tb.N, Tb.Th, and BVF.

Ex vivo bovine trabecular bone experiment

Sub-regional analysis for the MR T_2 and T_2^* values was conducted with high-resolution TSE Tb.Sp (which showed the highest correlation among the trabecular structural indices). The regional mean values of each sub-region were utilized for the correlation analysis. Figure 3.9 presents the results of bone marrow included ex vivo bovine trabecular experiments at multiple acquisition resolutions. The high-resolution TSE image and associated Tb.Sp map are presented in the first row of Figure 3.9A. The right parts of Figure 3.9A illustrates MR resolution dependency on MR transverse relaxation times. The T_2^* relaxation times are shortened as degrading acquisition resolutions, while the T_2 relaxation times maintains consistent values. The scatter plots for the resolution varying T_2 and T_2^* values regarding the values from high-resolution results are shown in Figure 3.9B. As the MR resolution decreased, the significant reduction of the dynamic range of the T_2^* was observed. As a result, the correlations for T_2^* was degraded. On the other hand, the dynamic range of T_2 relaxation times remained stable even with decreasing the imaging voxel size up to low-resolution of $1 \times 1 \times 1.25$ mm^3. Figure 3.9C observes the correlation coefficients between trabecular structural index of Tb.Sp with MR T_2 and T_2^* values in the view of MR acquitision resolutions. The decreasing T_2^* values resulting from degrading the MR resolution also weakened its correlation, while the T_2 values held strong correlation ($r > 0.82$, p-value < 0.001) with reference to Tb.Sp even at the low-resolutions until $1 \times 1 \times 1.25$ mm^3.

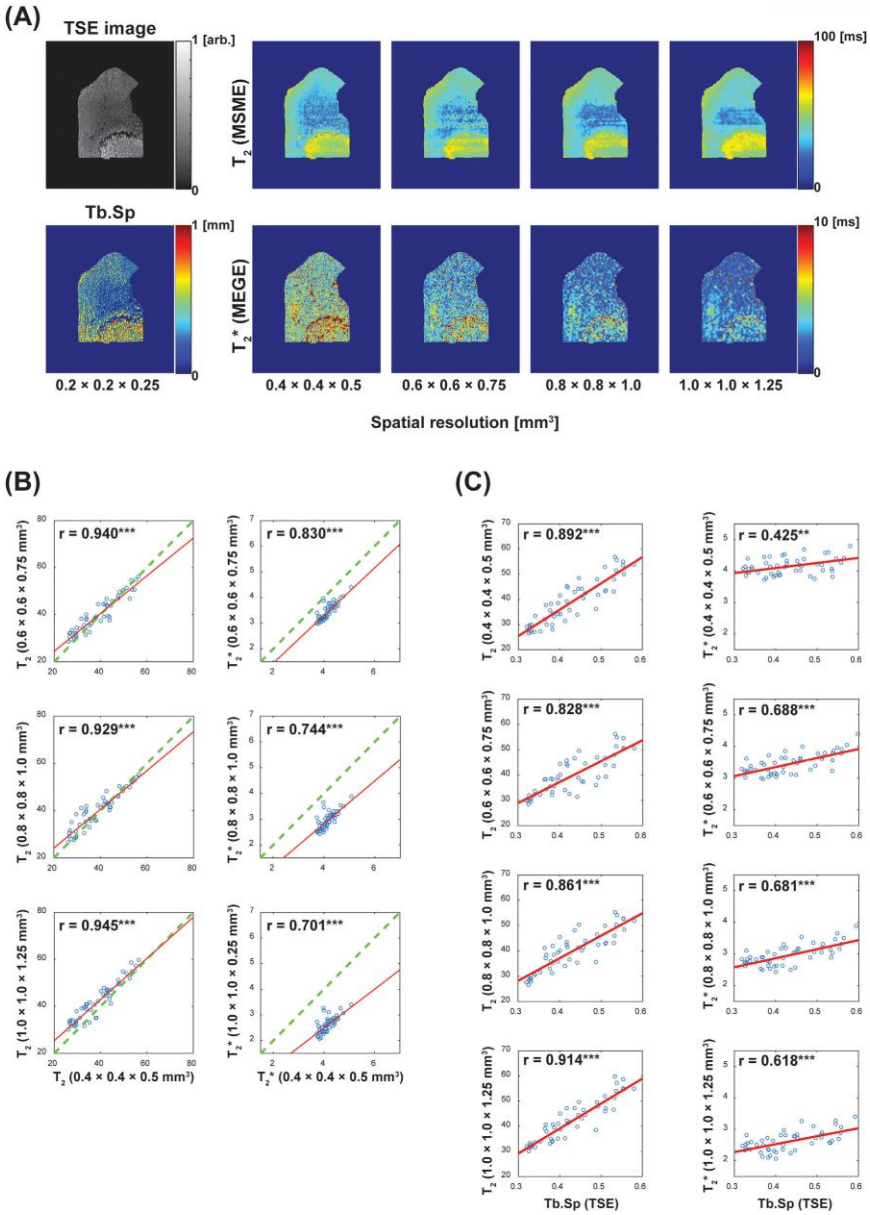

Figure 3.9 Correlation analysis for ex vivo bovine trabecular including marrow. (A) Anatomical trabecular image from TSE, associated Tb.Sp, and T_2, and T_2^* maps for multiple acquisition resolutions. (B) The resolution dependency of T_2 and T_2^* values. (C) Correlation coefficients of T_2 and T_2^* values with respect to TSE Tb.Sp.

The results for the bovine trabecular experiments (n = 4) is summarized in Figure 3.10 by means of scatter plots from multiple MR acquisition resolutions in reference with those from the MR resolution of 0.4 × 0.4 × 0.5 mm^3. The T_2^* values decreased apparently with degrading MR acquisition resolutions. Figure 3.10B presents the correlations for T_2 and T_2^* relaxations in reference with the TSE-derived Tb.Sp for various MR resolutions. The correlations for T_2^* gradually degraded with decreasing the acquisition resolution along with reducing absolute T_2^* values, which is in accordance

with the results for the defatted human trabeculae experiment. However, T_2 values at multiple MR resolutions kept strong correlations with high-resolution Tb.Sp.

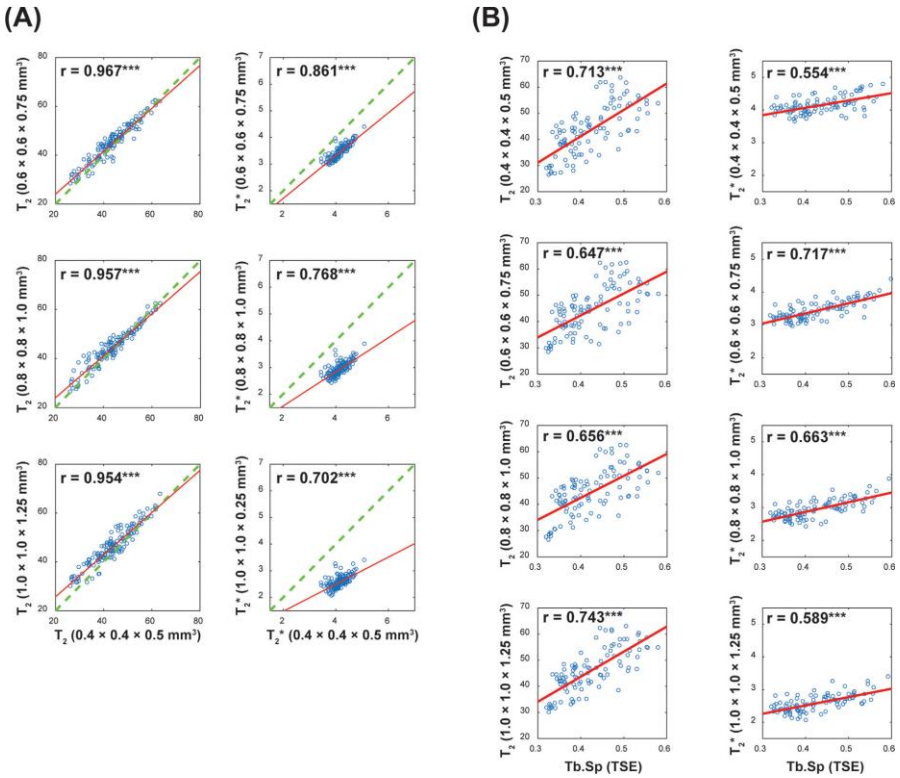

Figure 3.10 The resolution dependency of MR relaxation times from the ex vivo experiments for bone marrow included bovine trabeculae (n = 4) (A). Correlation coefficients for resolution-varying MR transverse relaxation times with high-resolution Tb.Sp at multiple MR resolutions (B).

3.4 Discussion

For the bone marrow removed human trabeculae experiment, the T_2 and T_2^* values provided stable and consistent correlations for micro-CT Tb.Sp with the MR resolution of 125 mm^3. The correlation coefficients for the T_2^* value with respect to the micro-CT trabecular structural indices degraded for the low acquisition resolutions. This is likely because of decreasing the dynamic value range of the T_2^* relaxation time. Therefore, in order to prevent the unwanted shortening of T_2^* values and corresponding dynamic ranges at the low spatial resolution, high-resolution MRI with long scan times may be still required at 7 T, which loss advantages of the reduction in scan-time against micro-MRI. However, T_2 relaxation times, which is often considered to be unresponsive to trabecular structural indices at clinical field strengths [15], guaranteed significant correlations with trabecular micro-structural indices at 7 T. This is presumably because of increasing magnetic susceptibility contrast at high field, without regard for the imaging voxel size. The resulting resolution dependency of MR

transverse relaxation times showed consistent behaviors with the corresponding MC simulation results. Accordingly, the results for the bovine trabeculae including marrow also provided a practical extension of low-resolution MR T_2 relaxometry for scan-time limited clinical application.

The resolution independent robustness of MR T_2 relaxation time can be interpreted as follows. The phase accumulation for a spin-echo acquisition (resulting in a T_2 relaxation) mostly presents near bone-marrow interfaces. On the other hand, the phase accumulation for a gradient-echo acquisition arises over a much broader region, even apart from the trabeculae. As presented in the second rows of Figure 3.2, the accumulated phases for the spin- and gradient-echo methods with increasing TEs support these expectations. Therefore, when the MR acquisition resolutions for gradient-echo method is sufficiently high, the reduced phase deviation inside the imaging voxel guarantees long T_2^* values and corresponding dynamic range with enough correlations to represent trabecular micro-structural information [28]. In the same manner, with degraded MR resolution of UTE acquisition, the T_2^* value is dramatically decreased, even apart from the surface. This is might because of significant dephasing of the diffusion protons in the bone marrows. However, T_2 relaxations are occurred particularly in the vicinity of the trabecular surface due to the short diffusion length (~ 8 mm) in the presence of magnetic field shifts. Therefore, MR T_2 relaxation time effectively maintains the micro-structural information regardless of a degraded acquisition resolution. The results for the bovine trabeculae experiments including bone marrow were consistently agreed with those of defatted human trabecular experiments. The correlations of T_2^* with respect to trabecular structural indices degraded as decreasing MR acquisition resolutions, while the reducing correlations were slower than that from the defatted trabecular experiments. The slow T_2^* relaxation of the bovine trabecular samples is mostly due to the restricted molecular diffusion length in the presence of adipose tissues in a marrow tissue. The T_2 relaxation times against MR resolution maintained absolute values and dynamic ranges ($r > 0.95$ for the resolution of $0.4 \times 0.4 \times 0.5$ mm^3 in 11 minutes) along with strong correlations especially for the Tb.Sp ($r > 0.7$ in reference to high-resolution TSE Tb.Sp within 22.5 minutes). Considering the reduced scan time of T_2 acquisition was 2 minutes with covering a large FOV of $60 \times 68 \times 12.5$ mm^3, low-resolution T_2 measurements might be beneficial to detect subtle changes of trabecular micro-architectures, when high-resolution (< 250 mm^2) anatomical micro-MRI is challenging along with enhanced SNR and further reduction in scan time.

The limitations of this study are described as follows. First, the MC simulation results for the behaviors of the MR relaxation times were analyzed without considering an adipose tissue distribution in a bone marrow. The effects of an adipose tissue in the bone marrow, such as reduced molecular diffusion length and the restricted water molecules in a high-gradient region, is crucial and under investigation [21,45,46]. Although T_2 and T_2^* values from bovine trabeculae experiments including bone marrow showed comparable observations both with defatted human trabecular experiments and MC simulations, further in vivo studies for more practical simulations with considering adipose

tissues may strengthen the robustness of the future study for the clinic. Second, even though the trabecular micro-structural indices Tb.Sp represents overall bone strength, mechanical tests and their correlations with the T_2 relaxation time should be examined in the future study. Third, no experiment data for the standard clinical field strength of 1.5 T and 3 T are introduced in this study. Therefore, the direct comparisons at 3 T may support in establishing the concrete benefits of low-resolution T_2 mappings over T_2^* measurement because T_2^* relaxation times are prone to the resolution at 3 T as well, which puzzle the utilizing T_2^* as a surrogate of trabecular micro-architectures.

As a conclusion, ex vivo T_2 relaxation time ensured consistent correlations for trabecular micro-architectural index, such as Tb.Sp, whereas T_2^* values and micro-MRI-derived trabecular structural indices were susceptible to decreasing MR acquisition resolution at 7 T. Enhanced T_2 relaxations at high magnetic field of 7 T may be utilized as a bone quality index together with dramatically minimized acquisition duration. This may be beneficial for the deep anatomic regions, such as hip and spine, where micro-MRI is challenging in clinics due to the insufficient SNR, large FOV, and unsuitably lengthy scan times.

4. Robust MRI size assessment of cerebral microvasculature using diffusion-time-dependent stimulated-echo acquisition

4.1 introduction

Measurements of the changes in magnetic resonance (MR) transverse relaxation rates induced by the injection of an intravascular contrast agent (ΔR_2 and ΔR_2^* from the spin-echo (SE) and gradient-echo (GRE) methods, respectively) enable the morphological quantification of cerebral microvasculature, such as blood volume fraction (BVf), mean vessel diameter (mVD), and vessel size index (VSI) [47–49]. The lower bound for vessel diameter quantification is largely determined by the diffusion length during encoding, magnetic susceptibility difference ($\Delta\chi$) between vessels and tissues, and magnetic field strength (B_0) [47,50]. The large $\Delta\chi$ values of intravascular superparamagnetic iron oxide nanoparticles (SPION) and shortened echo time (TE) under strong magnetic fields (> 7 T) satisfies the static dephasing regime without losing overall sensitivity for measuring MR relaxation rates [47]. Therefore, MR sensitivity and robustness for quantifying changes in small vessel radius can be enhanced. However, both increased magnetic field strength and $\Delta\chi$ worsen the effects of macroscopic field inhomogeneity and large vessel influences based on GRE acquisitions, which critically limits the robustness of conventional MRI measurements of vessel sizes for small cerebral microvasculature [33,51,52]. Additionally, the division of relaxation rate maps from separate GRE and SE acquisitions typically needs further adjustments from the inherently different $\Delta\chi$-dependence and the necessary co-registration of the two acquisitions. These issues are all significantly amplified under strong magnetic fields (> 7 T) for small rodent brains, which limits the robust quantification of cerebral vasculatures, especially in the vicinity of the olfactory bulb (OB) and cortex.

As a result, there is a growing need to develop an optimal MR method to enhance conventional GRE acquisition to obtain regionally robust ΔR_2^* values for relatively small cerebral vasculatures [33,52]. Stimulated-echo (STE; π/2-TE/2-π/2-TD-π/2-TE/2) imaging acquisition can monitor diffusive decay in the presence of inhomogeneous magnetic fields with well-defined diffusion times (TDs) for longitudinal magnetization. This method has been used to measure the pore sizes and surface-to-volume ratios of porous materials, such as trabecular bones, by measuring signal decay during TD [53,54]. However, to the best of our knowledge, no previous studies have applied the STE method to quantify the sizes of cerebral vasculature in vivo.

Susceptibility induced magnetic field variation exists over the length-scale of vasculatures. At long TDs for STE acquisition, water molecules diffuse sufficiently to lose significant correlations between

the magnetic fields at their initial and final positions, implying that the STE signal will directly reflect the ΔR_2^* contrast of the corresponding free induction decay (FID) [53]. Because the corresponding diffusion length is still shorter than the length over which the unwanted fields change, these unwanted fields are refocused. However, at small TDs, the contrast of STE acquisition resembles that of SE acquisition and the STE signal will produce ΔR_2 contrast. Consequently, with dual STE acquisitions at short and long TDs for a fixed TE, separate ΔR_2 and ΔR_2^* contrasts can be obtained without the confounding factors of GRE-induced image artifacts, such as air-tissue-interface-induced distortions and size overestimation caused by adjacent larger vessels. In addition, the same STE acquisition with only different TD removes the need of image registration and minimizes $\Delta\chi$-dependence between gradient and spin echo images.

In this study, we investigated the feasibility of employing the STE imaging method to simultaneously reduce the effects of macroscopic field inhomogeneity from air-tissue interfaces and vessel size overestimation to achieve regionally robust quantification of mean vessel diameter for rodent brains. First, STE-derived mVD was compared to the values acquired from conventional GRE and SE methods based on Monte-Carlo (MC) proton diffusion simulations in the presence of the susceptibility-induced magnetic field inhomogeneities of randomized cylindrical objects. Second, in vivo estimation of mVD based on STE for both short (10 ms) and long (600 ms) TD acquisitions for the white matter (WM), cortex, and OB of the brain were directly compared to the results of the conventional GRE and SE methods based on a 7 T system. All results were compared to reference knife-edge scanning microscope (KESM) [55] vasculature data with a 1-μm^3 resolution, which is considered to be the gold standard for mVD measurement, to evaluate the accuracy and robustness of STE-derived in vivo mVD.

4.2 Methods

ΔR_2, ΔR_2^*, and ΔR_{STE} simulations

MC simulations were performed to compute changes in MR transverse relaxation-rates (ΔR_2, ΔR_2^*, and ΔR_{STE} for SE, GRE, and STE, respectively) based on previously described procedures at a B_0 of 7 T [33]. The finite perturber method [32] was employed to calculate the B_0 shift of randomly distributed cylindrical models ($0.4 \times 0.4 \times 0.4$ mm^3) with various radii (each random cylinder model consisted with a single vessel radius; 2, 3, 4, 5, 6, 7, 8, 9, 10, 12, 20, and 30 μm) at BVfs (2, 4, 6, and 8 %) and a $\Delta\chi$ of 0.3 ppm (CGS unit) [56]. Identical calculations were performed at $\Delta\chi$ s (0.24, 0.36, and 0.48 ppm) and a BVf of 4%. The unit voxel size of the simulation was 1 μm^3 and the simulation

unit time (Δt) was 1 ms. Initially, 64,000,000 (400 × 400 × 400) protons were uniformly distributed inside the simulation volume (1 proton per unit voxel). The protons in the blood vessel region were removed to ignore the signal contributions of blood itself. The MC approach was employed with a periodic boundary condition for proton diffusion and a diffusion length of $\sqrt{2D\Delta t}$ (D is a diffusion coefficient equal to 1000 $\mu m^2 s^{-1}$) without vessel permeability for proton diffusion. To be specific, with each increment of Δt, the location of each proton is changed by N(0, 2DΔt) (independent normal random variates) with mean μ = 0, and standard deviation σ = $\sqrt{2D \cdot \Delta t}$ from (x, y, z) to (x+N(0,2DΔt), y+N(0,2DΔt), z+N(0,2DΔt)) (D is a diffusion coefficient equal to 1,000 $\mu m^2 s^{-1}$). The phase accumulation of each proton during the TE was calculated and the MR signal was determined by averaging the accumulated phases of all diffused protons. The phase accumulation of an nth proton during the time t, $\phi_n(t)$, was calculated as follows.

$$\Phi_n(t) = \sum_{j=1}^{\frac{t}{\Delta t}} \gamma \Delta B\big(p_n(j\Delta t)\big)\Delta t, \quad [4.1]$$

where γ = proton gyromagnetic ratio (267.5×10^6 rad/T), $p_n(t)$ = position of nth proton at time t, ΔB(p) = magnetic field shift at position p. The MR signal was determined by averaging the accumulated phase factors, that is $e^{i\varphi}$, across the entire ensemble of N diffusing protons.

$$S(t) = \frac{1}{N}\sum_{n=1}^{N} e^{i\phi_n(t)} \quad [4.2]$$

GRE, SE, and STE acquisitions were simulated with a TE of 10 ms. The TDs for STE were set to 10, 300, 600, 900, and 1200 ms. During the TD for STE acquisition (π/2-TE/2-π/2-TD-π/2-TE/2), the protons were diffused over a diffusion length of $\sqrt{2D \cdot TD}$ without phase accumulation because spins were aligned along the longitudinal direction during the TD. The phase coherence of STE acquisition (between dephasing during the first TE/2 and rephasing during the second TE/2) is modulated by adjusting the TD, which gradually lose coherence as the TD increases [53]. The changes in transverse relaxation rates were calculated using the following equation:

$$\Delta R_2,\ \Delta R_2^*,\ \text{and}\ \Delta R_{STE} = \frac{1}{TE}\ln\left(\frac{S_{pre}}{S_{post}}\right), \quad [4.3]$$

where S_{pre} (equal to one for MC simulation) and S_{post} are the signal intensity before and after administration of the contrast agent, respectively. The simulated mVR_{GRE} and VSI from the GRE and SE methods were evaluated [56].

$$mVR_{GRE} = \frac{\Delta R_2^*}{\Delta R_2} \quad [4.4]$$

$$VSI = 0.424\frac{\sqrt{D}}{\sqrt{\gamma\Delta\chi B_0}}\left(\frac{\Delta R_2^*}{\Delta R_2}\right)^{\frac{3}{2}} \quad [4.5]$$

The corresponding mVR_{STE} from the STE method ($\Delta R_{STE,\ TD=300ms\sim1200ms}/\Delta R_{STE,\ TD=10ms}$) at four different long TDs (300, 600, 900, and 1200 ms) were calculated.

$$mVR_{STE} = \frac{\Delta R_{STE,\text{long TD}}}{\Delta R_{STE,\text{minimum TD}} \text{ or } \Delta R_2} \quad [4.6]$$

Such mVR_{MRI}s (mVR_{GRE} and mVR_{STE}) and VSI values were obtained for various BVFs (2, 4, 6, and 8%) at fixed $\Delta\chi$ of 0.3 ppm. They were also obtained for various $\Delta\chi$s (0.24, 0.36, and 0.48 ppm) at a fixed BVF of 4% and TD of 600 ms. Then each mVR_{MRI} and VSI values were compared to the radii of randomly distributed cylindrical models. Each calculation was repeated ten times (n = 10) with randomized cylindrical models to obtain each standard deviation.

In vivo rat experiment

Animal experiments were approved by the Institutional Animal Care and Use Committee of the Ulsan National Institute of Science and Technology. All experiments were performed under anesthesia (5% isoflurane for induction and 2% for maintenance in 70% ambient air/30% oxygen). Body temperature was maintained by a circulating warm water tube positioned around the torso. To minimize the signal contribution from external encoding gradients during the TE, a STE sequence with a phase-cycling scheme was implemented on a Bruker 7 T scanner (ParaVision 6.0) [57]. The ΔR_2^*, ΔR_2, $\Delta R_{STE,TD=600ms}$, and $\Delta R_{STE,TD=10ms}$ values of healthy Wistar rats (n = 5) were measured using SE, STE, and multi-echo GRE acquisitions with the following parameters: pulse repetition time (TR) = 5000 ms, TE = 10 ms, number of scans = 4, acquisition resolution = 0.234 × 0.234 × 1 mm^3, number of slices = 3 (slice gap of 5 mm to cover the cortex, WM, and OB), and contrast agent dose = 360 μmol iron/kg using SPION. The TE for multi-echo GRE acquisition ranged from 2 to 46 ms (echo spacing of 4 ms) and the TE image at 10 ms was used for further analysis. ΔR_2^*, ΔR_2, and $\Delta R_{STE,TD=600ms}$ were calculated using Eq. 4.3 and the MRI mVD (mVD_{MRI}) and VSI were evaluated based on Eq. 4.4−4.6.

To determine the in vivo mVD_{MRI} using STE, $\Delta R_{STE,TD=10ms}$ was replaced with ΔR_2 to reduce the total scan time because ΔR_2 and $\Delta R_{STE,TD=10ms}$ provide consistent information, as discussed in the results section. The value of experimental $\Delta\chi$ was evaluated by measuring high-resolution steady-state ΔR_2^* values at cortex region ($\Delta\chi = \frac{3\,\Delta R_2^*}{4\pi\,BVf\,\gamma\,B0}$) with 2.9% blood volume fraction [56]. The value of diffusion constant was evaluated by measuring 3-direction averaged ADC values as shown in Figure 4.1.

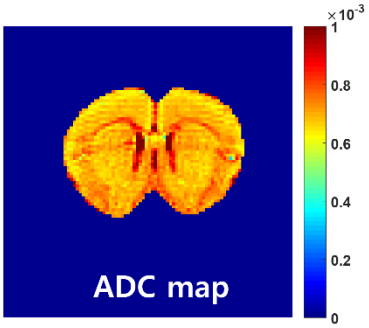

Figure 4.1 Representative 3-directional ADC values (mm^2s^{-1}) of a healthy Wistar rat.

Mouse cerebral microvasculature

To provide quantitative reference for MR measure of vessel sizes, three-dimensional mouse brain microvascular data was obtained from the KESM brain atlas (kesm.cs.tamu.edu/home/index.php). It should be noted that only reference mouse KESM data was available and calibrated (or normalized) comparisons were made between the rat MRI-derived vessel sizes and mouse KESM results. Because the ratio between the vessel radii of mouse cortex and corpus callosum regions was observed to be consistent with the corresponding ratio of rat brains (0.86 for KESM mouse brain vasculature and 0.85 for reported rat brain data [58]).The microvasculature was stained using an India-ink perfusion method and imaging was performed using KESM with an in-plane resolution of 0.6 × 0.7 μm^2 and a depth of 1 μm [59,60]. Raw microvascular data in scalable vector graphics file format were downloaded for a slice range of 1000–7500 (corresponding to a 6.5-mm-thick volume) and the microvasculature was converted into the portable network graphics file format. The vascular region was segmented via image thresholding. Next, the microvasculature was divided into 0.5-mm-thick volumes (500 slices per volume) and each volume was resized to an isotropic resolution of 1.0 × 1.0 × 1.0 μm^3. Three volumes corresponding to image slices from in vivo rat experiments were selected and voxel-based mVD based on KESM vasculature (mVD_{KESM}) was calculated using a 3D sphere-fitting method [38,39] in the BoneJ software package [40]. mVD_{KESM} values less than or equal to two were excluded from further analysis because the minimum mVD_{KESM} value from the 3D sphere-fitting method was two based on a unit voxel size of 1.0 × 1.0 × 1.0 μm^3.

Comparison between mVD_{KESM} and mVD_{MRI}

To compare KESM and MR images (using SE images prior to injection), three brain regions, namely the corpus callosum and associated subcortical WM, neocortex (NC), and OB, were manually segmented by referencing the Scalable Brain Atlas [61]. Regional mVD_{STE} values were first evaluated.

Each regional mVD_{STE} was multiplied by a scaling factor ($\frac{\text{mean}(mVD_{KESM,WM})}{\text{mean}(mVD_{STE,WM})}$) to obtain calibrated mVD_{STE}. The calibration of mVD_{STE} are based upon the simulation results that that mVD_{KESM} and mVD_{STE} are semi-linear in this radius range. Correspondingly, regional mVD_{GRE} and VSI_{GRE} were evaluated and compared with mVD_{KESM}.

Next to minimize vessel size variations in different animals, in vivo mVD_{MRI} values (ΔR_2^* / ΔR_2 and $\Delta R_{STE,TD=600ms}$ / ΔR_2) were normalized relative to the mean (or median) values of mVD_{KESM} in the WM ($\text{normalized } mVD_{MRI} = \frac{mVD_{MRI}}{\text{mean}(mVD_{MRI,WM})} \times \text{mean}(mVD_{KESM,WM})$). VSI values were also accordingly normalized. Then, the mVD_{KESM} and normalized mVD_{MRI} values for the WM, NC, and OB regions were compared by means of a normalized frequency histogram, cumulative function, and scatter plot of mean (median) values with minimized inter-animal variations.

4.3 RESULTS

MC simulation

Representative MC simulation results for randomly distributed cylindrical models are depicted in Figure 4.2 and Figure 4.3. The randomness of the cylinder orientation decreases as the cylinder radius increases, which most likely causes the increases of standard deviation at larger radius. The phase accumulations of $STE_{TD=10ms}$ largely occur in the near-surface region with a randomly spread pattern, similar to those of SE. The phase accumulations of $STE_{TD=1200ms}$ show comparable behavior to those of GRE around the cylinder region, which is likely a result of the long diffusion length of $\sqrt{2D \cdot TD}$ ≈ 50 μm in the simulations. The degree of phase accumulation of the $STE_{TD=1200ms}$ simulation tends to decrease over a cylinder radius of approximately 10 μm as shown in Figure 4.2.

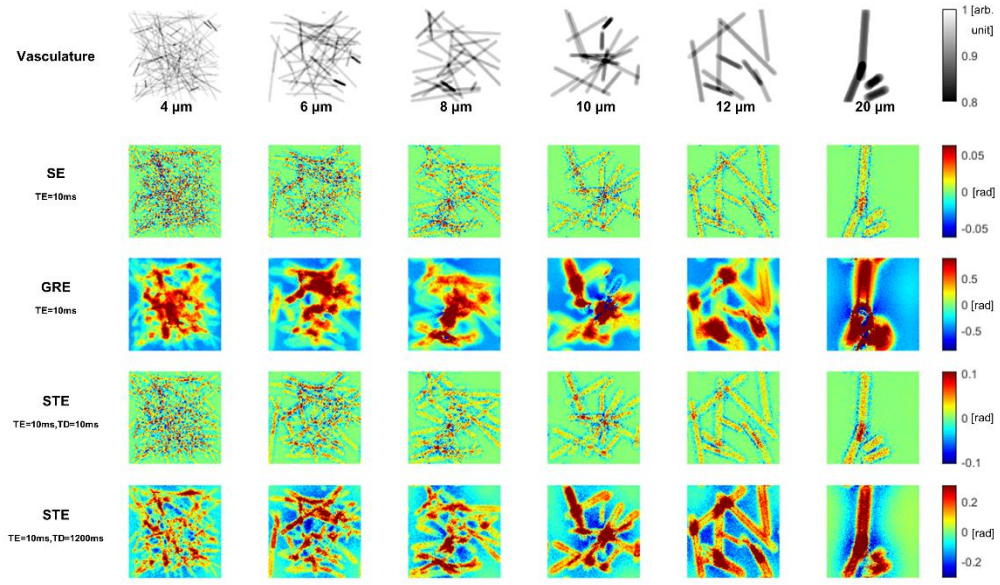

Figure 4.2 MC proton diffusion simulation of the changes in MR relaxation rates caused by an intravascular contrast agent at 7 T. The phase accumulations of GRE, SE, and STE acquisitions were computed to those of randomly distributed cylindrical models. Representative images of randomly distributed cylindrical models and computed phase accumulations of each acquisition.

Figure 4.3 illustrates the computed changes in relaxation rates and corresponding mVD_{MRI} values. ΔR_2^* and $\Delta R_{STE,TD=1200ms}$ are proportional to the BVf changes and remain relatively constant compared to ΔR_2 as the cylinder radius increases. The standard deviation of ΔR_2^* (Figure 4.3A-1) increases as the cylinder radius and BVf increase, while $\Delta R_{STE,TD=1200ms}$ (Figure 4.3B-1) appears to remain stable. $\Delta R_{STE,TD=1200ms}$ gradually decreases for large cylinder radii over 10 μm at a rate slightly higher than that of the corresponding ΔR_2^* value. ΔR_2 and $\Delta R_{STE,TD=10ms}$ exhibit an inverse relationship with cylinder radius. $\Delta R_{STE,TD=10ms}$ is slightly larger than ΔR_2 due to the TD of 10 ms in the simulation. The computed mVD_{GRE} (Figure 4.3A-2, $\Delta R_2^* / \Delta R_2$), VSI (Figure 4.3A-2, $0.424\frac{\sqrt{D}}{\sqrt{\gamma\Delta\chi B0}}(\frac{\Delta R2*}{\Delta R2})^{3/2}$), and mVD_{STE} (Figure 4.3B-2, $\Delta R_{STE,TD=600,1200ms} / \Delta R_{STE,TD=10ms}$) values were observed to be proportional to the cylinder radius with minimized contributions from blood volume. Specifically, for small cylinder radii below 10 μm, mVD_{STE} was observed to show smaller standard deviations compared to mVD_{GRE}, regardless of different blood volumes. However, for cylinder radii larger than 10 μm, mVD_{STE} was more consistent, but appeared to underestimate vessel diameters as blood volume increased. The computed mVD_{GRE}, VSI, and mVD_{STE} values (Figure 4.3A-3 and Figure 4.3B-3) were also observed

to be proportional to the cylinder radius at various $\Delta\chi$ values (0.24,0.36, and 0.48 ppm) at fixed blood volume fraction (4%). Specifically, mVD_{STE} values were observed to exhibit minimized contributions from $\Delta\chi$ variations. Furthermore, the adjustment of mVD_{STE} values by $\sqrt[4]{\Delta\chi}$ (instead of $\sqrt[2]{\Delta\chi}$ for conventional VSI) was observed to further compensate $\Delta\chi$-dependence of TD-varying STE acquisitions up to radius of 10 μm in estimating vessel sizes (Figure 4.3B-3).

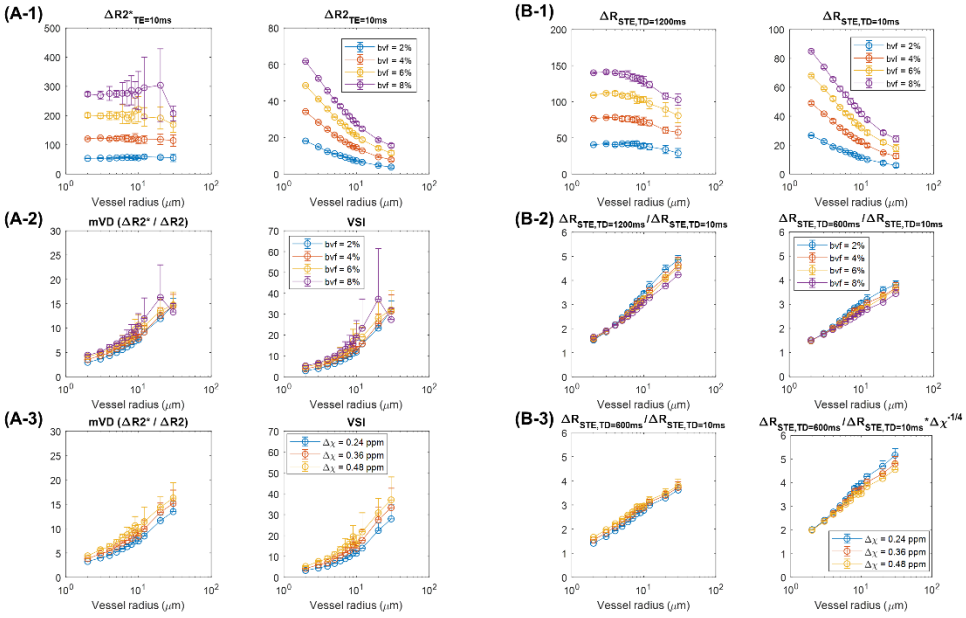

Figure 4.3 Changes in MR relaxation rates (ΔR_2^*(TE = 10ms), ΔR_2 (TE = 10ms), and ΔR_{STE} (TE = 10ms, TD=1200ms and 10ms) for GRE, SE, and STE methods, respectively (A-1 and B-1). Conventional MRI mVD_{GRE} and VSI were shown (A-2). Suggested mVD_{STE} values of different long TD values ($\Delta R_{STE,TD=1200ms}$ / $\Delta R_{STE,TD=10ms}$ and $\Delta R_{STE,TD=600ms}$ / $\Delta R_{STE,TD=10ms}$) were shown (B-2).

In vivo rat experiment

Figure 4.4 depicts in vivo measurements of cerebral ΔR_2^* and $\Delta R_{STE,TD=600ms}$ values. The length of the TD (600 ms, diffusion length of $\sqrt{2D \cdot TD} \approx 34$ μm) was chosen by considering an appropriate signal-to-noise ratio (SNR) and capillary diameter of a rat brain, whose mean values are less than 5 μm [62]. One can observe that ΔR_2^* is dominantly affected by large vessels (especially large penetrating vessels in the NC region) and underestimated by B_0 inhomogeneity near the skull (the GRE_{pre} signal itself was distorted by air-tissue interfaces and the skull).

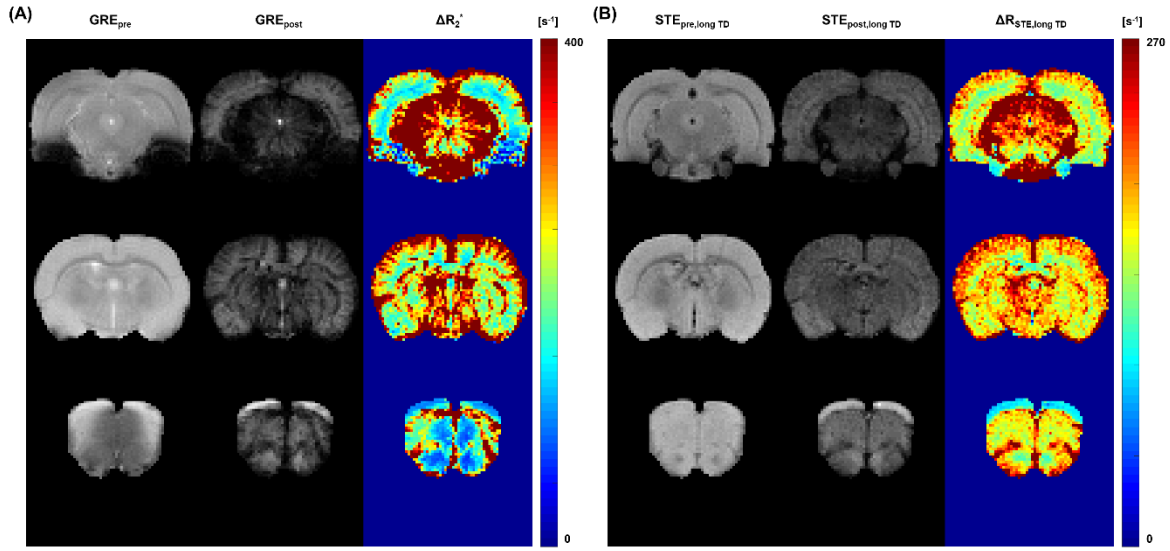

Figure 4.4 In vivo changes in MR relaxation rates (ΔR_2^* and ΔR_{STE} for GRE and STE methods, respectively) for a healthy Wistar rat (208 g). ΔR_{STE} with a long TD shows comparable results to ΔR_2^* without image distortion based on macroscopic field inhomogeneity and large vessel overestimation.

In contrast, $\Delta R_{STE,TD=600ms}$ is barely affected by macroscopic field inhomogeneities based on the SE-like rephasing of STE acquisition. The in vivo ΔR_2 and $\Delta R_{STE,TD=10ms}$ values exhibit similar relaxation rates and consistent contrast, as shown in Figure 4.5. One can see that $\Delta R_{STE,TD=10ms}$ is slightly larger than ΔR_2, which is consistent with the results of MC simulation.

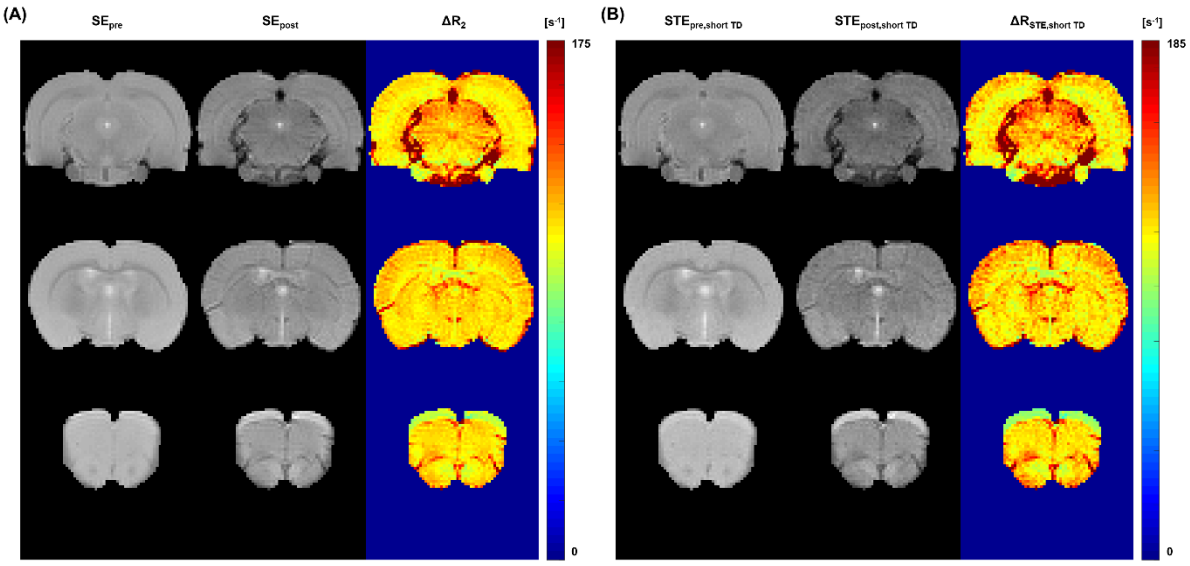

Figure 4.5. In vivo changes in MR relaxation rates (ΔR_2 and ΔR_{STE} for SE and STE methods, respectively) for a healthy Wistar rat (208 g). ΔR_{STE} with a short TD shows comparable results to ΔR_2.

In vivo mVD_{GRE}, VSI, and mVD_{STE} values are mapped in Figure 4.6. The vivo results are comparable to the results of MC simulation. Specifically, one can see that mVD_{GRE} and VSI values are underestimated in areas with macroscopic field inhomogeneity based on severe air-tissue interfaces, as indicated by the white arrows. In contrast, mVD_{STE} appears to be robust to the air-tissue interface artifacts in rodent brains. The values of mVD_{GRE} are larger than those of mVD_{STE} in the areas around penetrating large vessels in the cortex, as shown in the middle row.

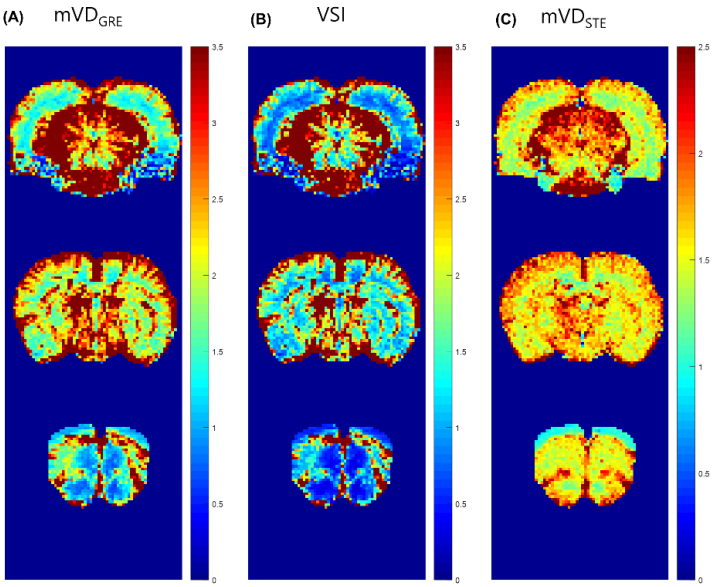

Figure 4.6 In vivo results of GRE- and SE-based MRI mVD_{GRE} ($\Delta R_2^*/\Delta R_2$) (A), VSI (B) and mVD_{STE} ($\Delta R_{STE,longTD}/\Delta R_2$) (C) for a Wistar rat (208 g). The mVD of the STE method (C) shows comparable results to that of the GRE method (A,B) without image distortion caused by macroscopic field inhomogeneity and large vessel overestimation (white arrows).

Reference cerebral microvasculature

A representative mouse microvasculature and the calculated mVD_{KESM} method are visualized in Figure 4.7. Figure 4.7A presents the KESM vasculature corresponding to a single 0.5-mm-thick volume. As shown in Figures 4.7B and 4.7C, BVf and mVD_{KESM} exhibit a clear difference between the NC and WM regions. Both the mVD_{KESM} and BVf values of the NC region with penetrating vessels are larger than the those of the WM region.

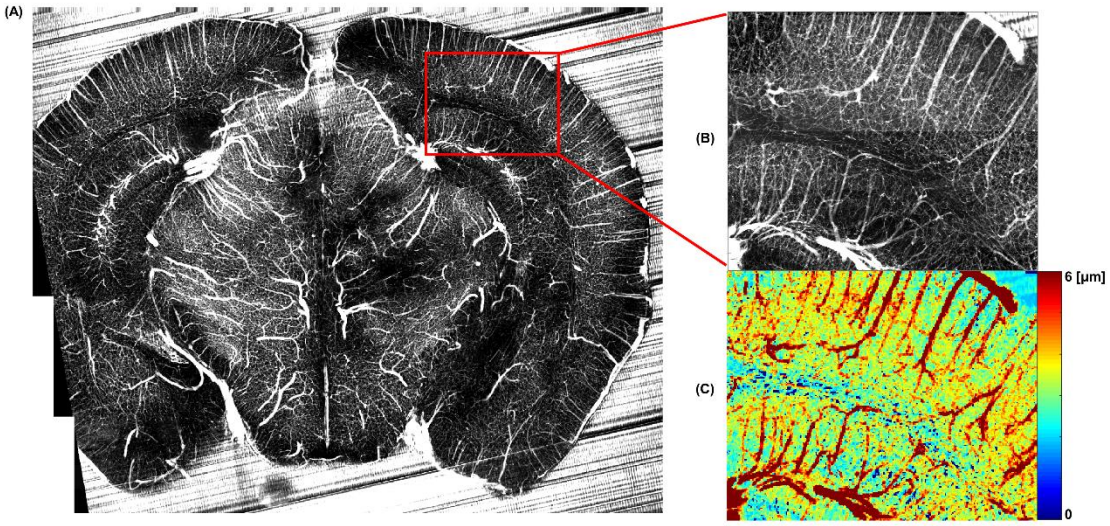

Figure 4.7 (A) Three-dimensional mouse brain microvascular data from the KESM Brain Atlas. (B) BVf of the cortex and WM regions, and corresponding mean vessel diameter map calculated using a sphere-fitting method.

Comparison between mVD_{KESM} and mVD_{MRI}

Figure 4.8A presents regional (WM: red, OB: blue, and Cortex: green) scatter-plot comparisons (mean values) of mVD_{STE} (Figure 4.8A-1) calibrated mVD_{STE} (Figure 4.8A-2), mVD_{GRE} (Figure 4.8A-3), and VSI (Figure 4.8A-4) values (n = 5) with respect to mVD_{KESM}. The values mVD_{STE} were smaller than those of mVD_{KESM}, and consistently followed the marked blue line ($y=\frac{\text{mean}(mVD_{STE,WM})}{\text{mean}(mVD_{KESM,WM})}x$). Then, subsequently calibrated mVD_{STE} was in good agreement ($r = 0.69$, $p < 0.005$) with respect to mVD_{KESM}. The values of mVD_{GRE} and VSI showed reduced linearity ($r= 0.57$ and 0.56, $p < 0.05$) with respect to mVD_{KESM}. Under- and overestimations of vessel sizes in OB and cortex regions were respectively observed. To further remove potential vessel size variations among each animal, each value was normalized with respect to the corresponding value of WM region of same animal as described in the method section. Improved linearity ($r = 0.85$, $p < 0.001$) of normalized mVD_{STE} with respect to mVD_{KESM} was observed in comparison with normalized mVD_{GRE} ($r = 0.65$, $p < 0.01$) and normalized VSI ($r = 0.63$, $p < 0.05$). Under- and overestimations of vessel sizes in OB and cortex regions were still conspicuous.

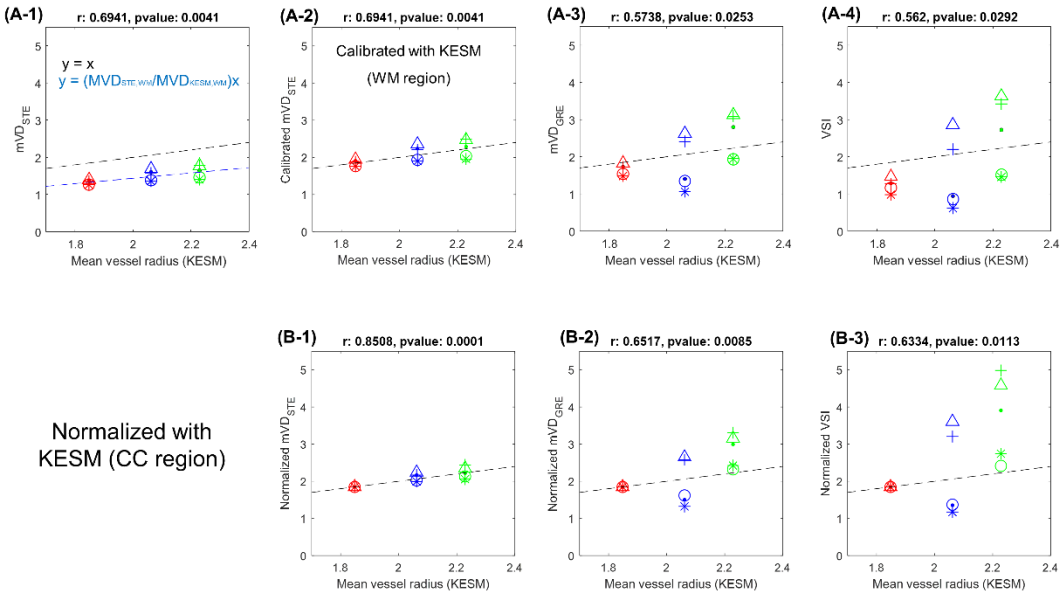

Figure 4.8 Comparison between mVD values from KESM and MRI mVD_{STE} (A-1), calibrated mVD_{STE} (A-2), mVD_{GRE} (A-3), and VSI (A-4). Normalized mVD_{STE} (B-1), mVD_{GRE} (B-2), and VSI (B-3) are also shown to reduce vessel size variations among animals.

Figure 4.9 presents comparison results between distributions of mVD_{MRIS} (n = 5) and mVD_{KESM}

values. The regions of interest (ROIs) for MRI and KESM vasculature are highlighted in Figure 4.9A and Figure 4.10, respectively. Normalized frequency histograms of mVD_{KESM}, normalized mVD_{STE}, and normalized mVD_{GRE} are compared in Figures 4.9B-1, 4.9B-2, and 4.9B-3, respectively. As described in Eq. 3, mVD_{MRI}s values were normalized relative to the median of mVD_{KESM} in the WM region. For mVD_{KESM} and normalized mVD_{STE}, the median of each ROI is similar, and the median of the WM region is smaller than those of the NC and OB regions. In contrast, normalized mVD_{GRE} in the OB region exhibits an underestimated median value based on macroscopic field inhomogeneity caused by air-tissue interfaces. Compared to mVD_{KESM}, the median of normalized mVD_{GRE} in the NC region is relatively overestimated based on the presence of large penetrating vessels. The cumulative functions show consistent results (Figure 4.9C). For normalized mVD_{GRE} (Figure 4.9C-3), an intersection in the cumulative function occurs at a small radius due to the underestimation in the OB region. Saturation of the cumulative function of normalized mVD_{GRE} in the NC region is slower than that of mVD_{KESM} due to the overestimation in the corresponding region. The cumulative function of normalized mVD_{STE} generally matches that of mVD_{KESM}, while the normalized mVD_{STE} appears to lose some of large vessel information, which is likely caused by the decreasing $\Delta R_{STE,longTD}$ values of large vessel radii based on the limited length of the TD, as shown in the corresponding MC simulations. The vessel size overestimation in the NC and underestimation in the OB of the normalized mVD_{GRE} are conspicuous, but the size estimations based on normalized mVD_{STE} are consistent with respect to mVD_{KESM} in the scatter plot of median values (n = 5), as shown in Figure 4.9D-1 and 4.9D-2.

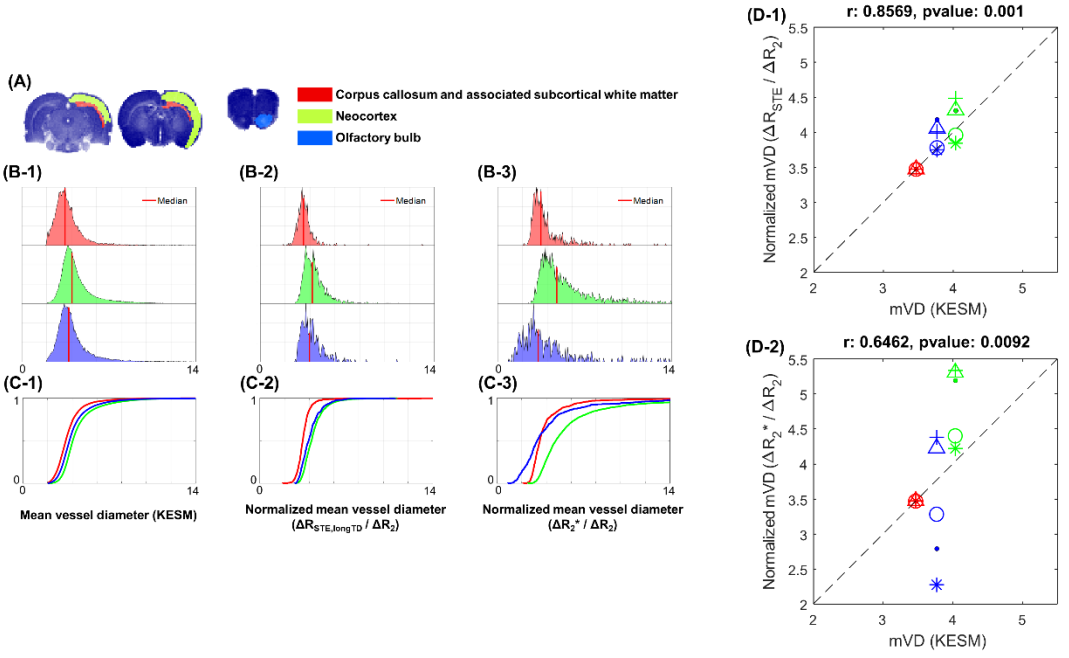

Figure 4.9 Comparison between mVD values from KESM and MRI mVDs (mVD_{GRE} and mVD_{STE} from ΔR_2^* / ΔR_2 and $\Delta R_{STE,longTD}$ / ΔR_2, respectively). MRI results from rat brains (n = 5) were combined for analysis. (A) Three ROIs from pre-injection SE images. (B) Frequency-normalized histograms and (C) cumulative functions of the KESM, normalized mVD_{STE}, and normalized mVD_{GRE} were compared for the three ROIs. By referencing the mVD values from KESM, the scatter plots of mVD_{STE} and mVD_{GRE} were compared for the three ROIs.

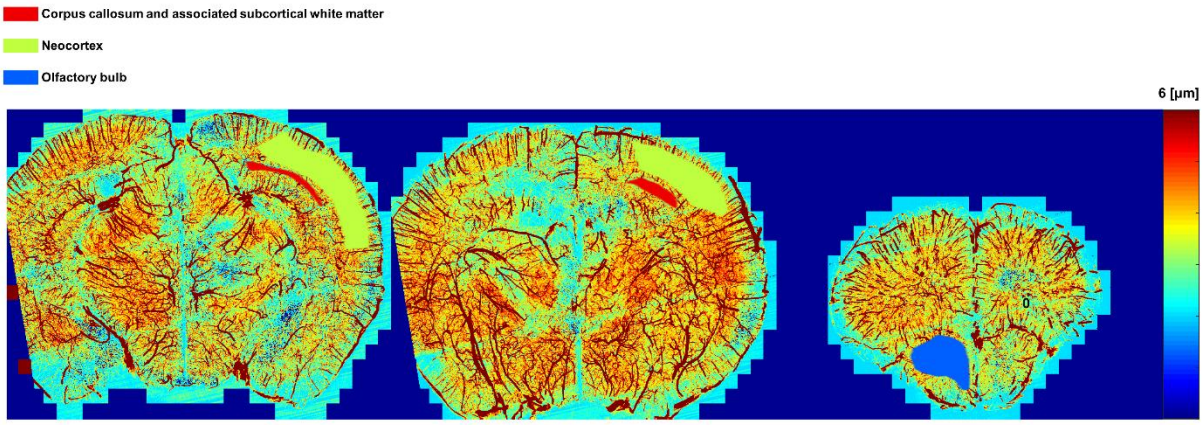

Figure 4.10 (B) Mouse vasculatures and (A) corresponding mVD maps from the KESM Brain Atlas. Three ROIs were selected to match the result ROIs for in vivo MRI.

4.4 Discussion

As a method for overcoming the limitations of conventional GRE and SE combined acquisitions for MR measurement of vessel diameter, the feasibility of the proposed STE diffusion imaging method was demonstrated through MC simulations and in vivo rat experiments using a 7 T system, focused on accurately quantifying small microvessels. The MC simulations revealed that changes in MR relaxation rates based on STE acquisition (ΔR_{STE}) provide the vessel diameter information by

regulating the length of the TD. The microvessel-related information of ΔR_{STE} between long and short TDs was comparable to that of the GRE and SE methods, respectively. The ΔR_{STE} value with a long TD tended to decrease at large cylinder radius (radius > 10 μm), which supports the in vivo observations that macroscopic field inhomogeneities from large vessels, air-tissue interfaces, and the skull are reduced by the STE method. Experimentally, in direct comparisons to the KESM method using India-Ink blood vessel staining, both underestimation caused by macroscopic field inhomogeneity in the OB region and the influences of penetrating large vessels (or pial cortical veins) in the NC region of GRE-based vessel sizes were observed to be significantly reduced in the STE-based relaxation rate with a long TD. However, it should be noted that this poses a limitation for STE acquisition in terms of underestimating larger cerebral vasculature. Correspondingly, the in vivo mVD_{STE} value of $\Delta R_{STE,longTD}$ / ΔR_2 was successfully obtained and observed to be robust compared to the conventional mVD_{GRE} and VSI_{GRE} values in WM, OB, and cortical regions of rodent brains. These results were corroborated by the corresponding gold-standard mVD_{KESM} results.

It should be noted that absolute vessel size quantification from STE acquisition is still required with rigorous analytical approaches. Various Monte-Carlo simulation with varying blood volumes, size, and $\Delta\chi$ values in this study provided insights to asymptotic behavior of TD-dependent behavior of STE acquisition for vessel size estimation. However, due to potential discrepancies in the simulation approach, the analytical formula is used for absolute quantification of the conventional vessel size imaging, which also corresponds to STE acquisition. In this study, we specifically aimed to demonstrate the feasibility and benefits of STE acquisition for quantifying small vessel in OB and cortex areas, where conventional methods are known to suffer. As a result, the experimental mVD_{STE} values was calibrated (or normalized) in the white matter region with respect to the corresponding KESM results, without rushing absolute quantification based on only simulation results. In order to investigate the feasibility of absolute quantification of vessel size with TD-dependent STE acquisition, we must explore rigorous analytical derivation at different encoding regimes of STE acquisition along with extensive simulations. This is considered to be beyond the scope of current feasibility study.

There are potential adjustments for improvements related to the STE method for measuring mean vessel size. First, the signal strength of STE acquisition is half that of SE acquisition and T_1 relaxation during the TD (proportional to $e^{-TD/T1}$) reduces the SNR as the TD becomes longer. However, to obtain purely FID-like contrast from STE acquisition, the diffusion length (34 μm for TD = 600 ms in our experiment) during the TD should be sufficiently larger than the length of coherent susceptibility field variations due to cerebral vasculature of subject brains. Therefore, tradeoffs between SNR and ΔR_2^* contrast from varying TDs should be considered for potential clinical applications with larger vessel sizes (20,21). Figure 4.11 shows TD (300ms, 600ms, 900ms, and 1200ms) dependent behavior of vessel size estimation for this purpose.

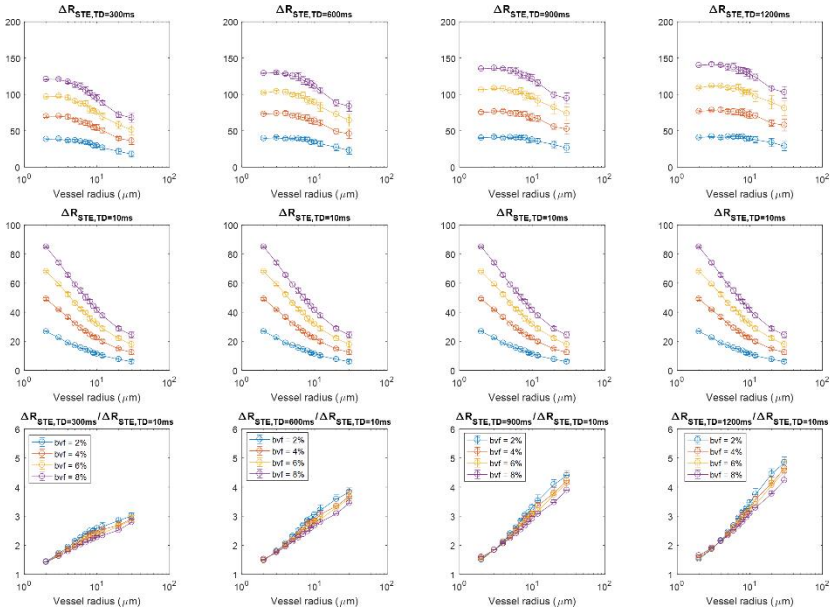

Figure 4.11 TD dependent simulation results for STE-based vessel size estimations.

Since capillary radius in human cerebral cortex is 3.23±0.85μm [63], the minimum TD value over 600ms appears to be necessary from simulation results for clinical applications. Second, to cover the entire imaging region, the TR for STE_{longTD} should be lengthened based on the TD and multi-slice acquisition, which increases the total scan time and sensitivity to motion artifacts because the signal encoding duration of the STE method (TE + TD) is longer than that of GRE acquisition (TE). Limitations based on the SNR and elongated scan time of STE acquisition can be resolved by using multiple array coils and acquisition acceleration techniques, such as compressed sensing and parallel acquisition [64]. Third, the possibility of obtaining vessel size distribution information from a single image voxel remains to explored with TD varying STE acquisitions. With well-regulated diffusion length from TD at fixed TE, the Laplace inversion of STE signal decay as a function of TD can potentially provide vessel size distribution from image voxel [53].

In conclusion, TD-dependent STE-based MR relaxation rates ($\Delta R_{STE,longTD}$ and $\Delta R_{STE,shortTD}$) provide a robust measure for assessing the size of small cerebral microvasculature without co-registering GRE and SE acquisitions, especially where macroscopic field inhomogeneity and large vessel contaminations are significant with only STE acquisitions.

5. Optimization of sparse phase encodings for variable repetition-delay turbo-spin echo T_1 measurements

5.1 Introduction

Measuring an absolute in vivo MR T_1 relaxation times provides accurate and precise assessments of tissue micro-environments, and moreover offers non-invasive physiological surrogates for diagnosis of diseases and monitoring therapy effects [65–67]. Although inversion-recovery [68] and saturation-recovery [69] spin-echo acquisitions have been considered as gold-standards for MR measures of the T_1 relaxation, the impractically long required scan times often restricts their operation for clinical or even for preclinical applications.

Thus, fast-readout MR pulse sequences are normally employed with reduced acquisition duration for the MR T_1 measurement, which usually involve multiple-excitations with single-inversion Look–Locker [70–72] and multiple-flip-angles with steady-state techniques [73–75]. However, fast MR acquisitions with these techniques are generally vulnerable to artificial image distortions and inaccurately estimating T_1 values which mostly occurred from B_0 inhomogeneities and flip-angle dependency of repeated excitation pulses. And these shortcomings are routinely emphasized for the applications of high field (> 7 T) clinical and preclinical research due to both increasing B_0 inhomogeneities and corresponding radio frequency (RF) together with RF power deposition in the body of examine patients [76].

To overcome these limitations typically occurred from the gradient-echo based methods, a spin-echo acquisition with multiple-refocusing-pulses, that is a turbo-spin-echo (TSE) [77], is commonly utilized for the assessments of the MR T_1 relaxation by using varying pules repetition-times (TRs) together with well-defined signal models. Moreover, the spin-echo method is especially beneficial for the high-field preclinical MRIs, where the RF-deposition is uncritical and B_0 inhomogeneities are severely influence both the imaging and mapping qualities of the MR T_1 relaxation time. However, applying TSE-based methods for the preclinical MRI research is sometimes hindered from (1) decreasing signal intensity and broadening point-spread-function distortion due to T_2 relaxations during echo-trains of TSE methods which especially emphasized for the conditions of short T_2. (2) Inter-slice interferences (such as inter-slice cross-talks and magnetization transfer effects) from multi-slice excitations accompany with (3) lengthened scan-times due to multiple-TRs are also responsible for the limiting the usage of TSE methods even for preclinical researches, where small sizes of organs of interests often restrict the slice-gaps [78]. Accordingly, capabilities of parallel imaging techniques

are also limited on account of the inadequately small field-of-view (FOV) as well as expensive multiple-array-coils.

Recent advances in MR acquisition techniques assisted from sparse sampling strategies provide dramatically reduced total acquisition time of multi-dimensional MRI [64,79,80]. Several researches have been conducted to demonstrate the feasibilities for various MR parameters with these techniques [81–85]. Thus, a multi-slice T_1 mapping with variable TR TSE acquisitions together with the sparse sampling strategies may provide a reasonable solution for preclinical researches.

In this study, we systematically explored the advantages of applying a compressed-sensing (CS) technique to multiple-TR TSE methods for the preclinical measurements of the MR T_1 relaxation time. The effects of sparse sampling of MR phase-encodings and CS reconstruction were optimized for Gd-DOTA (DOTAREM) phantoms with various concentrations, ex vivo, and in vivo T_1 measurements at 7 T.

5.2. Methods

T_1 fitting procedures

By adopting a centric echo-order phase-encoding schemes for the TSE acquisition, the signal behavior of a TSE method [86] can be generalized at certain TF with minimized T_2 relaxations:

$$S_{TSE} = S_0\left\{1 + \sum_{n=1}^{TF} 2(-1)^n e^{(-TR+TE*\frac{(2TF-n+1)}{2})/T_1} + 2(-1)^{TF-1} e^{\left(-\frac{TR}{T_1}\right)}\right\}, \quad [5.1]$$

where S_0 is the proton spin density, and TE is the echo-time (echo-spacing in this case) between the initial 90 º excitation pulse and the first echo. The summation term describes the repeating 180 º refocusing pulses which continuously reverse the longitudinal magnetization, Mz, resulting in reduced recovery time of the longitudinal magnetization, which effectively reduce the TR proportional to the echo-spacing and echo-train-length of the TSE acquisition [87].

The gold-standard T_1 relaxation times is fitted from inversion-recovery spin-echo (IRSE) acquisitions as follows [86].

$$S_{IRSE} = S_0\left(1 - 2e^{-\frac{TI}{T_1}} + 2e^{-\left(\frac{TR-TE/2}{T_1}\right)} - e^{-\frac{TR}{T_1}}\right), \quad [5.2]$$

where TI is the inversion time. The T_1 fittings were conducted using the MATLAB curve-fitting toolbox.

Sampling scheme optimization

Eight Gaussian-weighted randomly scattered sampling schemes for TSE acquisitions were generated along with incoherence to the TR direction at various fixed number of phase encodings in the low-frequency region of the k-space. To be more specific, the maximum priority of the sampled regions of the k-space was guaranteed to the fixed center k-space regions during the generation procedure of the sampling scheme, which is described in the previous study [88]. Each portion of the fixed center regions was set to 59, 49, 39, 31, 25, 19, 11, and 5. The single Gaussian-weight ($\sigma^2 = 0.125$) was used for the remaining part of the sampling scheme.

Because actual undersampled k-space data for a CS-TSE method are unable to be retrospectively acquired by subsampling a TSE data, the simulated k-space signals for the eight sampling schemes were utilized for the optimization of sampling schemes using the following equation:

$$S(k_x, k_y) = \sum_{y=1}^{FOV_y} \sum_{x=1}^{FOV_x} \rho(x,y) f_{T1}(x,y) f_{T2}(x,y) e^{-i2\pi(\frac{k_x x}{FOV_x} + \frac{k_y y}{y})}, \quad [5.3]$$

where $f_{T1}(x, y)$ is a function for the T_1 relaxation of the MR signal described with Eq. 5.1, and $f_{T2}(x, y) = e^{-TF \times TE / T2(x, y)}$ is used for the T_2 relaxation during the echo-trains.

The T_1 relaxation time and proton density for the sampling scheme optimization were acquired from multiple-TI IRSE data with the same acquisition parameters for the ex vivo rat-kidney experiment. The corresponding T_2 relaxation value was obtained from a multi-slice multi-echo spin-echo data with following MR parameters: TR of 7500 ms, echo-spacing of 8 ms, and number of echo-images of 32. By using these MR parameter values, the simulations for the various-TR CS-TSE acquisitions were performed to optimize the MR parameters for ex vivo and in vivo experiments.

The optimizations for each sampling scheme are conducted with the simulated CS-TSE images from CS reconstruction of the simulated k-spaces. Accordingly, the T_1 maps for the simulated CS-TSE images were generated, and the optimal sampling scheme was determined by choosing the maximum concordance correlation coefficients (CCC) [89] with respect to the standard input T_1 map from the IRSE experiment. In addition, the number of necessary TRs to maintain a reasonable T_1 map quality was examined with various number of TRs for all sampling schemes.

The image reconstruction strategy for the TR-varying CS-TSE data is described as following constrained optimization problem:

$$\text{minimize } \|\Psi s\|_1 \quad [5.4]$$

$$\text{subject to } \|Fs - k\|_2 < \varepsilon, \quad [5.5]$$

where s represents the sequence of images in the TR direction, and ψ is a linear operator to transform s into sparse domains of 2D wavelet and 1D Fourier domains in the x–y and TR directions, respectively. F is the Fourier operator of the optimal undersampling scheme and k is an obtained CS-TSE data. ε controls the fidelity of the CS image reconstruction, which is normally set below the noise level in the acquired k-space [64,90]. All the image reconstructions were conducted with MATLAB R2015a (MathWorks, Natick, MA, USA) environment. Additional external toolkits were also employed: spgl1 v.1.8 [91] and Wavelab v.8.02 [92] for the l1-norm minimization and for the wavelet transform, respectively. The data processing for this study was executed on a personal computer with an Intel Core i7-5960X 3.00 GHz central processing unit and 64 GB of memory running on Windows 7 operating system.

The effect of T_2 relaxation time on CS-TSE T_1 mapping

In order to investigate the effects of MR T_2 relaxation on a conventional TSE and proposed CS-TSE methods for the T_1 measurements, the additional simulations were performed with variously scaled input T_2 maps (original T_2 map × 1/4, 1/3, 1/2, 1, 2, 3, and 4). The image reconstruction for the CS-TSE was performed and followed by the T_1 mapping as described above. Accordingly, the CCC values for both TSE and CS-TSE methods were evaluated and compared with respect to the T_2 values to examine the advantages of substituting the echo-trains of conventional TSE acquisition with sparse samplings to reduce the effect occurred from MR T_2 relaxation.

Gd-DOTA phantom experiment

All experiments were conducted on a Bruker's 7 T MRI system. A 40 mm transceiver volume coil was used for the phantom experiment. To examine the T_1 measuring accuracy together with the T_1 fitting model for the CS-TSE method, absolute T_1 relaxation times obtained from CS-TSE acquisition were compared with conventional TSE acquisition in respect of reference T_1 values from IRSE method for six Gd-DOTA-doped saline solutions (0.15, 0.31, 0.62, 1.25, 2.50, and 5.00 mM). The T1 values of the Gd-DOTA phantoms ranged from 35 ms to 800 ms. The MR acquisition parameters for IRSE method is following: ten TIs (ranging from 25 ms to 7500 ms), TR of 7600 ms, TE of 8 ms, acquisition matrix of 256 × 256, FOV of 32 × 32 mm^2, and slice thickness of 1 mm. The TSE and CS-TSE experiments were performed with sixteen logarithmically increasing TRs (the ranges of TRs starting from 38, 70, 135, and 265 ms to 7500 ms for TFs = 4, 8, 16, and 32, respectively), a TE (echo spacing) of 8.2 ms, centric phase encoding order, and fourfold undersamplings (obtain 25% of the k-space) for the CS-TSE acquisitions. Mean T_1 relaxation times for each phantom was determined by averaging the T_1 values in the region-of-interest (ROI) and directly compared in respect of mean T_1 values for the IRSE acquisition.

Ex vivo experiments

A 23 mm transceiver volume coil was utilized for the ex vivo rat kidney experiment. The Institutional Animal Care and Use Committee of the Ulsan National Institute of Science and Technology approved the animal experiments performed in this study. A kidney from a Sprague–Dawley rat was harvested by clearing the blood in the vessels by a heart perfusion procedure, and immediately fixed in a formalin solution. Twenty-four hours later, the kidney was transferred into a 5 mL syringe with the formalin solution and fastened to prevent a mechanical motion during the MRI scan.

First, the accuracy of the T_1 maps for the conventional TSE and CS-TSE were examined by measuring single- and multi-slice T_1 maps with the ex vivo rat kidney phantom. Accordingly, to compare the measured T_1 values of the TSE and the CS-TSE methods, standard T_1 maps were evaluated by performing single-slice IRSE acquisitions for the corresponding slices. The identical MR acquisition parameters were employed for the ex vivo experiment with minor modifications as following: FOV of 16 × 16 mm^2, minimum TI of 100 ms for the IRSE, minimum TR of 180 ms, TFs of 2 and 8 for the TSEs (TSE2 and TSE8, respectively), and TF of 2 for the fourfold undersampled CS-TSE (CS4-TSE2). Five slices (n = 5) was used, which was enough to cover most of the morphological features of the ex vivo rat kidney.

The calculated CCC values with respect to the IRSE T_1 maps were used to compare the T_1 mapping qualities for the TSE and the CS-TSE acquisitions. The CCC values of the TSE and the CS-TSE for the same scan time or the same acceleration factor (TF × CS undersampling factor) were compared for the further analysis. Next, the increase in slice coverage of CS-TSE method compared with TSE, which relatively reduce the total scan time for the multi-slice T_1 measurement, eight-slices T_1 mappings were conducted with TSE2 and CS4-TSE2 acquisitions with the same number of total RF excitations per TR. Then, the CCC values for the result T_1 maps were accordingly calculated and compared. The scan time of the eight-slice CS4-TSE2 was 1/4 of that of corresponding eight-slice TSE2.

In vivo experiment

A 72 mm transmit volume coil and a mouse receive-only brain surface coil were utilized for the in vivo mouse abdomen T_1 measurements with BL6 mice. In a similar manner used for the ex vivo experiment, the multi-slice (two- and eight-slices) T_1 maps for TSE and CS-TSE with the same total scan time (total acceleration factor of 8 was used) were compared with reference to the TSE acquisition with TF of 2. The FOV for the in vivo mice abdomen experiment was 32 × 32 mm^2 (enough to cover the entire body). Other acquisition parameters were same as used for the ex vivo rat kidney experiment. The back-muscle and kidney regions (cortex and pelvis) were manually

segmented. The ROI-based mean T_1 relaxation times for each region were calculated and compared with respect of that from reference TSE2.

5.3. Results

Sparse sampling optimization

Figure 5.1 compares the multi-slice sampling schemes for the conventional TSE and proposed CS-TSE acquisitions together with accompanying advantages. The red lines in the black squares illustrate the sampled k-space regions for the corresponding pulse sequences. Both TSE and CS-TSE acquisitions employed a centric phase encoding order to reduce the T_2 relaxations of the signal by assigning the first echoes on the center of the k-spaces. Consequently, the low-frequency of the k-spaces for TSE8 and CS4-TSE2 acquisitions were assigned with the almost identical number of the first echoes (Figure 5.1A). On the other hand, for the high-frequency regions of the k-spaces for CS4-TSE2 had a shorter echo-trains together with relieved T_2 relaxations than those for TSE8. Thus, the reduced T_2 relaxation effects of the CS4-TSE2 acquisition minimized the inter-slice interferences of multi-slice acquisition and made room for additional slice encodings while holding a reduced scan time by a factor of four than conventional TSE2 as shown in Figure 5.1.

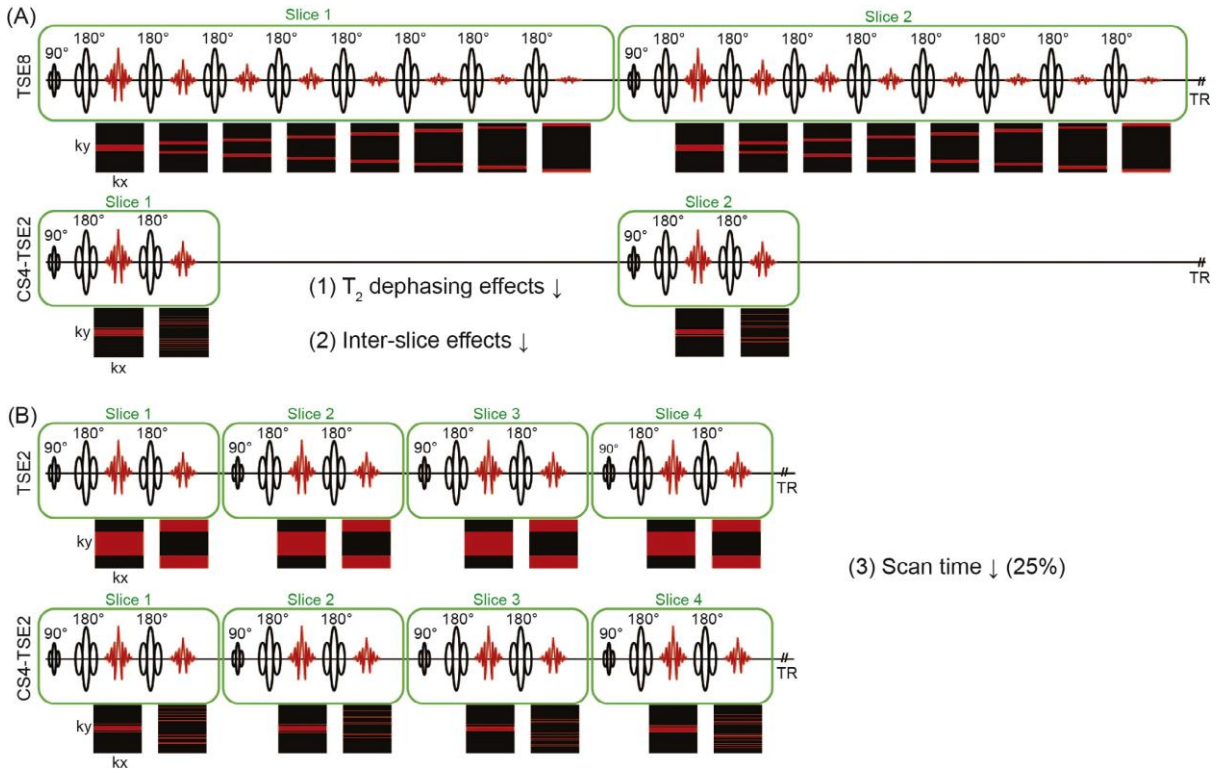

Figure 5.1 The benefit of employing CS technique on conventional TSE acquisition. To reduce the T_2

relaxation effects for a high signal-to-noise ratio and accurate T_1 fitting, both TSE and CS-TSE acquisitions utilized a centric-phase encoding scheme. The reduced echo-trains of CS-TSE acquisition minimized the repeated refocusing pulses at a fixed scan time compared with TSE acquisition (A). Reduced number of phase encodings for the CS-TSE method results in the scan time reduction for multi-slice T_1 mapping at fixed number of RF pulses per TR (B).

The sampling scheme optimization for the CS-TSE acquisition is illustrated in Figure 5.2. Briefly, the undersampled k-spaces for the CS-TSE acquisitions were generated from the proton density, T_1, and T_2 values of the ex vivo rat kidney experiments based on the sampling schemes with various portions of low-frequency signals (as shown in Figure 5.2A and 5.2B). The image reconstruction for the CS-TSE acquisitions were performed with additional pre-process to increase the transform sparsity in the TR direction. The rearrangement of the TR order for the CS-TSE to the bell-shape profile resulted in reduction of the necessary Fourier components in TR-domain as illustrated in Figure 5.3.

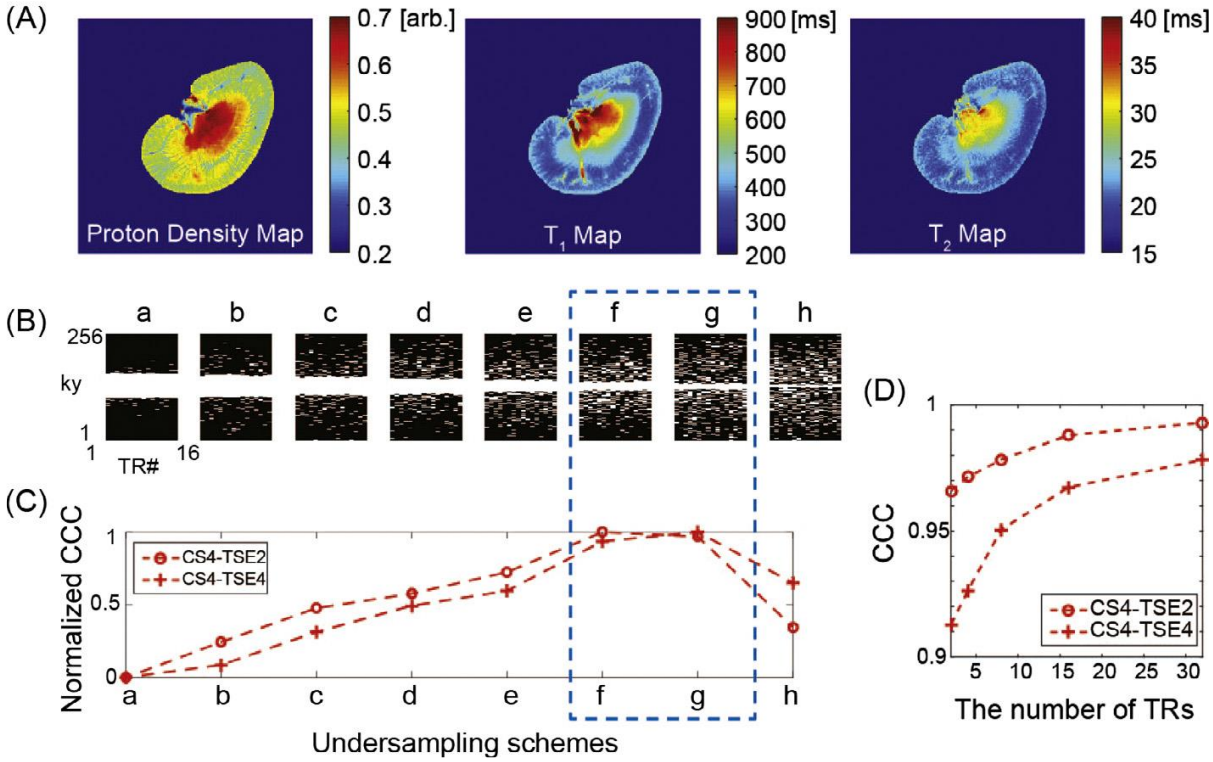

Figure 5.2 Sampling scheme optimization for variable-TR T_1 mapping with TSE sequence. Two-dimensional undersampling schemes for ky and TR directions were optimized regarding a number of fixed phase encodings for the center region of the CS-TSE k-space (B). With reference to the experimentally acquired MR parameter maps (A), the optimal undersampling scheme for the multi-slice T_1 mapping with CS-TSE acquisition was determined as marked with the blue dotted box (C).

The required number of TRs for the CS-TSE acquisition was optimized by evaluating the CCC values with respect to the reference input T_1 maps from IRSE acquisition (D).

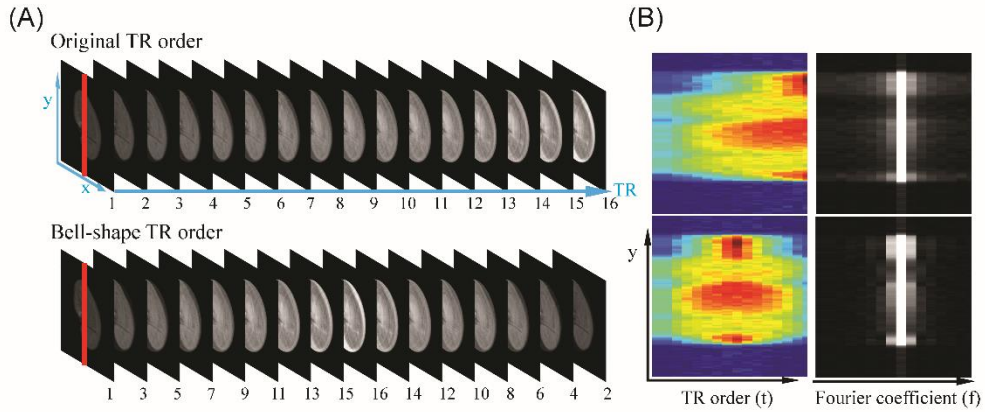

Figure 5.3 Enhancing the transform sparsity by rearranging TR order. Due to periodicity property of Fourier transform, TR images were rearranged to bell-shape order (A) in the sparsifying transform step of image reconstruction in order to reduce high frequency components of the first and the last TR images (B).

With the reconstructed CS-TSE images, the T_1 maps of each undersampling schemes were estimated. The CCC values of the corresponding T_1 maps were calculated with respect to the gold standard IRSE T_1 map. Each CCC value for the sampling schemes was normalized for the range from 0 to 1, and optimal undersampling schemes for the CS-TSE T_1 mapping was fixed (blue dotted box in Figure 5.2C), which sufficiently included the low-frequency regions of the k-space. Figure 5.2D summarized the optimization results of the necessary number of TRs for CS-TSE T_1 mapping. The CCC value of the CS-TSE T_1 map enhanced as increasing the number of TRs together with a saturating behavior with the number greater than approximately fifteen for the logarithmic time spacing. Thus, sixteen TRs were decided to be the optimal number of TRs for further simulations and experiments.

T_1 map reconstruction simulation at multiple T_2 values and acceleration factors

The effects of the intrinsic T2 values of the measured sample on the T1 mapping for conventional TSE and proposed CS-TSE acquisitions were explored by performing the similar simulation, and the results of the simulation was shown in Figure 5.4. The representative undersampling schemes for the simulations were shown in Figure 5.4A. The total acceleration factors for the TSE and the CS-TSE methods was set to 8 and 16 with almost identical echo distributions of the first echoes in the low-frequency k-space region due to the fixed center region strategy of the optimal schemes. The CCC values for the CS-TSE were decreased due to both T_2-related broadening but mainly resulting from

the image blurring of CS reconstruction, while the degradation of the CCC values for the TSE was mainly caused by the T_2 relaxation of the later echoes. The CCC values for both the TSE and the CS-TSE shows the highest values at the long T_2 values. However, for the short T_2, the quality of T_1 map for the CS-TSE is superior to that of the TSE at the same total acceleration factor (Figure 5.4B).

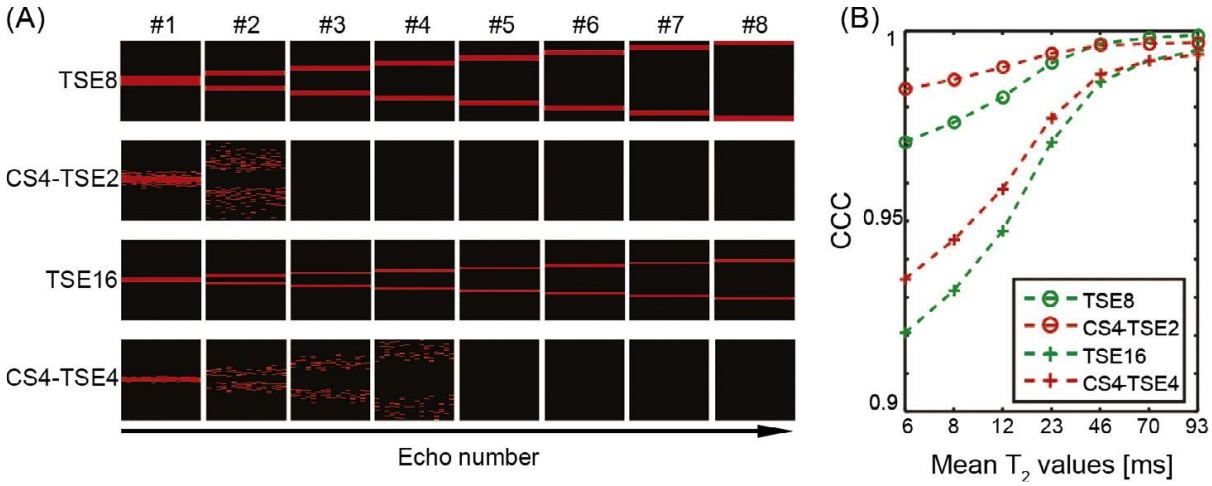

Figure 5.4 Increasing correlations with reduced T_2 decay effects of CS-TSE. The representative undersampling schemes for the TSE and the CS-TSE acquisitions at the same total acceleration factors are illustrated (A). The evaluated CCC values for both the TSE and the CS-TSE acquisitions are plotted according to the input T_2 values (B).

Phantom experiment

The ROI-based mean T_1 values for the Gd-DOTA phantom experiments are described in Table 5.1. The measure T_1 values for the TSE and the CS-TSE at all Gd-DOTA concentrations were compared with reference to those values from the gold standard IRSE acquisition. The turbo factors were examined from 4 to 32, and the CS acceleration factor for the CS-TSE was fixed at 4. The maximum values of the percentage T_1 differences for the TSE and CS-TSE acquisitions were 3.7% and −3.4%, respectively. Neither the sparse sampling nor the CS reconstruction of the CS-TSE produced discernible T_1 errors in the Gd-DOTA phantom experiments.

Table 5.1 The T_1 measuring accuracy of the TSE and the CS-TSE methods with respect to IRSE. Percentage T_1 differences were evaluated at the multiple concentrations of Gd-DOTA doped solutions. The T_1 relaxation times from both the TSE and the CS-TSE shows consistent measurement accuracy with respect to the gold standard IRSE.

		IRSE	TSE4	TSE8	TSE16	TSE32	CS4-TSE4	CS4-TSE8	CS4-TSE16	CS4-TSE32
	Total scan time	5 h 24 min	20 min	10 min	5 min	3 min	5 min	3 min	2 min	1 min
	#RF pulse in TR	3	5	9	17	33	5	9	17	33
0.15 mM	T_1 [ms]	770.8	793.1	791.2	798.0	799.2	791.6	787.9	795.5	793.1
	Pct. diff. T_1 [%]		-2.9%	-2.6%	-3.5%	-3.7%	-2.7%	-2.2%	-3.2%	-2.9%
	R^2	0.9976	0.9998	0.9998	0.9998	0.9998	0.9997	0.9998	0.9999	0.9998
	Adj. R^2	0.9973	0.9998	0.9998	0.9998	0.9998	0.9997	0.9998	0.9999	0.9998
0.31 mM	T_1 [ms]	480.8	480.9	488.3	491.9	491.2	481.0	486.3	494.7	484.5
	Pct. diff. T_1 [%]		0.0%	-1.6%	-2.3%	-2.2%	0.0%	-1.1%	-2.9%	-0.8%
	R^2	0.9987	0.9996	0.9998	0.9998	0.9998	0.9997	0.9998	0.9997	0.9997
	Adj. R^2	0.9985	0.9996	0.9997	0.9998	0.9998	0.9997	0.9998	0.9997	0.9997
0.62 mM	T_1 [ms]	269.7	274.1	272.0	272.9	274.2	275.8	273.3	272.7	270.8
	Pct. diff. T_1 [%]		-1.6%	-0.8%	-1.2%	-1.6%	-2.3%	-1.3%	-1.1%	-0.4%
	R^2	0.9987	0.9998	0.9997	0.9998	0.9998	0.9998	0.9998	0.9999	0.9999
	Adj. R^2	0.9985	0.9998	0.9997	0.9998	0.9998	0.9998	0.9998	0.9999	0.9999
1.25 mM	T_1 [ms]	147.7	148.5	149.6	149.8	149.3	150.0	150.2	151.2	148.7
	Pct. diff. T_1 [%]		-0.6%	-1.3%	-1.4%	-1.1%	-1.6%	-1.7%	-2.4%	-0.7%
	R^2	0.9998	0.9998	0.9999	0.9999	0.9998	0.9998	0.9999	0.9998	0.9996
	Adj. R^2	0.9997	0.9998	0.9999	0.9999	0.9998	0.9998	0.9998	0.9998	0.9995
2.50 mM	T_1 [ms]	77.8	76.9	76.9	76.3	76.7	75.2	76.0	76.9	76.4
	Pct. diff. T_1 [%]		1.1%	1.2%	1.9%	1.4%	3.4%	2.2%	1.1%	1.8%
	R^2	0.9999	0.9996	0.9997	0.9997	0.9996	0.9996	0.9998	0.9997	0.9996
	Adj. R^2	0.9999	0.9995	0.9996	0.9997	0.9996	0.9995	0.9998	0.9996	0.9996
5.00 mM	T_1 [ms]	38.4	38.7	38.6	39.2	38.9	39.1	39.0	38.7	38.6
	Pct. diff. T_1 [%]		-0.7%	-0.6%	-2.1%	-1.4%	-1.9%	-1.6%	-0.8%	-0.6%
	R^2	0.9992	0.9996	0.9996	0.9996	0.9996	0.9997	0.9996	0.9996	0.9995
	Adj. R^2	0.9991	0.9996	0.9996	0.9996	0.9995	0.9997	0.9996	0.9996	0.9995

Ex vivo kidney experiment

The results of the ex vivo rat kidney experiment were summarized in Figure 5.5 and Table 5.2. The reference T_1 map for the ex vivo experiments are shown at the upper left side in Figure 5.5A. The results for the single-slice T_1 measurements shows that the T_2 relaxation effects of the TSE on the accuracy of the measured T_1 in the absence of inter-slice interferences. Only the T_1 mapping accuracy for the TSE8 was significantly degraded due to the long echo-train from TF of 8, while the TSE2 and CS4-TSE2 showed consistent T_1 values with respect to the reference T_1 from IRSE. At the same time, the total scan time for the CS4-TSE2 was 1/4 of that of the conventional TSE2 without losing the accuracy.

For the results of the multi-slice T_1 measurements, the T_1 values of TSE8 were significantly overestimated in comparison with that from TSE2 and CS4-TSE2 acquisitions. The T_1 overestimation of TSE8 is largely contributed by the inter-slice interferences of long echo-train-length. Accordingly, the accuracy of the T_1 measurement of the CS4-TSE2 is compatible with the corresponding TSE2 with the reduced total scan time of four, while the specificity of the measured T_1 maps are degraded due to the image blurring from the CS image reconstruction. The results of the eight-slices T_1 measurements clearly depicted the scan time reduction of the CS-TSE acquisitions with extended slice coverage. The overall accuracy of the eight-slices T_1 maps from CS4-TSE2 were consistent with the that from TSE2, while the overestimation of measured T_1 from both the TSE2 and the CS4-TSE2 were significant because the large number of applied RF pulses per TR enhanced the inter-slice interferences.

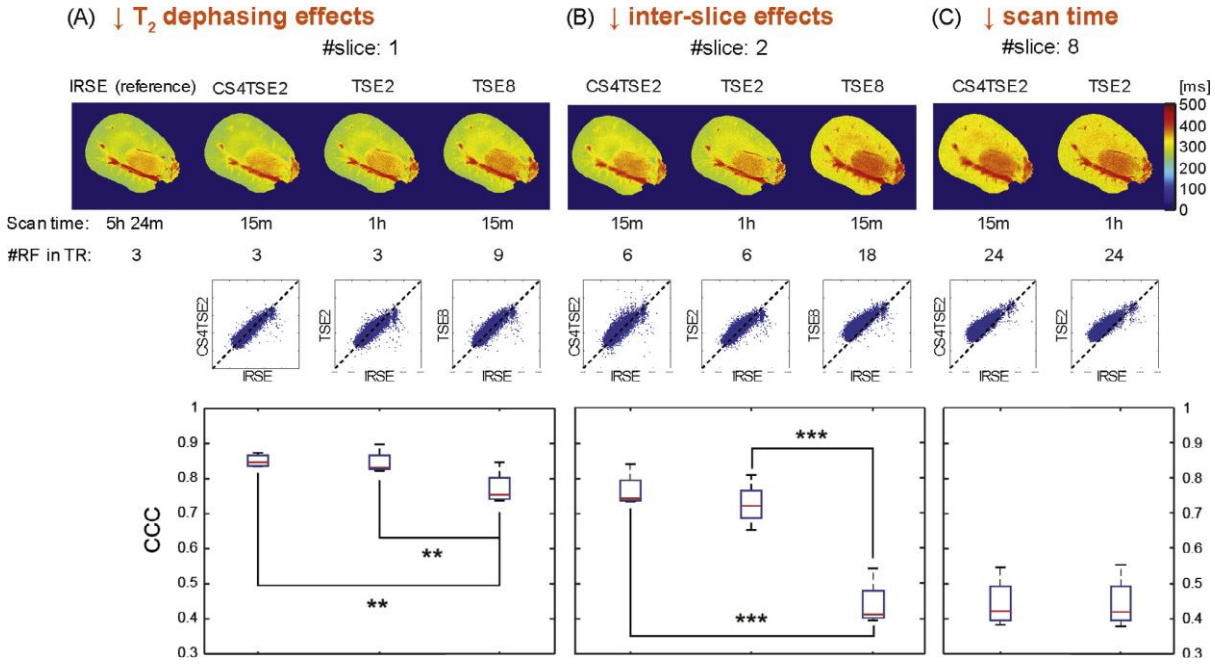

Figure 5.5 The T_1 mapping accuracy for TSE and CS-TSE with respect to IRSE for ex vivo rat kidney experiments (n = 5). Measured T_1 maps for the single- and multi-slice acquisitions were shown in the first row, and corresponding scatter plots and the CCC values were presented, respectively. single-slice CS4-TSE2, TSE2, and TSE8 acquisitions (A); two-slice CS4-TSE2, TSE2, and TSE8 acquisitions (B); and eight-slice CS4-TSE2 and TSE2 acquisitions (C).

Table 5.2 The evaluated T_1 mapping quality and corresponding significant matrix for the ex vivo rat kidney experiments. The p values were calculated by employing two-sided paired-two-sample t-test. * $p < 0.05$; ** $p < 0.01$; *** $p < 0.001$

					p value				
					#slices 1		#slices 2		#slices 8
		n	CCC Mean	CCC SD	CS4-TSE2	TSE8	CS4-TSE2	TSE8	CS4-TSE2
#slices 1	TSE2	5	0.8282	0.0436	0.5607	0.0018**			
	CS4-TSE2	5	0.8329	0.0362		0.0067**			
	TSE8	5	0.7455	0.0653					
#slices 2	TSE2	5	0.6805	0.1030			0.0607	0.0002***	
	CS4-TSE2	5	0.7393	0.0655				0.0000***	
	TSE8	5	0.4090	0.0824					
#slices 8	TSE2	5	0.4236	0.0708				0.7950	0.6974
	CS4-TSE2	5	0.4216	0.0714				0.8224	

In vivo experiment

The in vivo results of the multi-slice T_1 mappings for the mice abdomen was summarized in Figure 5.6 and Table 5.3. For the back muscle and cortex and pelvis regions of the in vivo mice kidney, the T_1 maps, corresponding ROI-based mean T_1 values, and the results of the statistical tests are illustrated in Figure 5.6. In accordance with the results of the ex vivo phantom experiments, the mean T_1 values for

the CS4-TSE2 acquisitions showed comparable results with those from the TSE2 acquisition. Accordingly, the mean T_1 values of TSE8 were significantly overestimated with respect to both the TSE2 (for the back-muscle and pelvis regions) and CS4-TSE2 (for the back-muscle, cortex, and pelvis regions), while only two-slices T_1 mapping was conducted. The image blurring of the T_1 map from the CS4-TSE2 acquisition was noticeable due to the CS image reconstruction.

For the results of eight-slice T_1 mapping, both TSE2 and CS4-TSE2 showed consistent measured T_1 values for all regions as listed in Table 5.3, whereas the total scan time of the CS4-TSE2 was 1/4 of that of the TSE2 acquisition. Several overestimations of the T_1 relaxation times for all three regions were found for both acquisitions because of multiple RF excitation pulses.

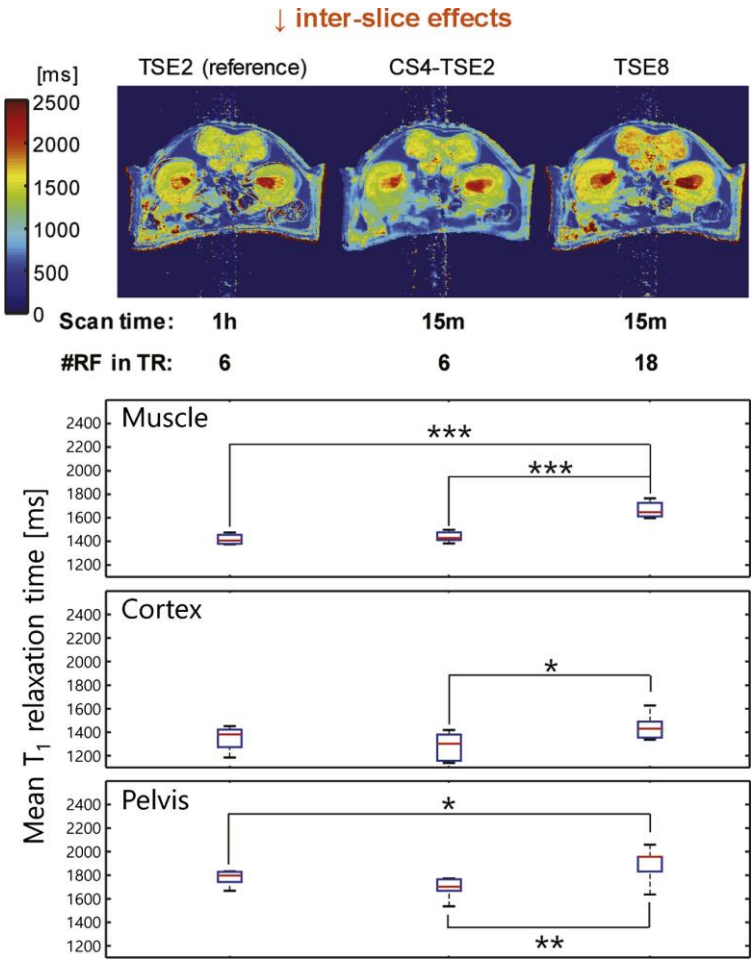

Figure 5.6 In vivo results of the two-slice T_1 mappings for mice abdomen. The representative T_1 maps and ROI-based mean T_1 values of back-muscle, kidney cortex, and kidney pelvis regions.

Table 5.3 Statistical analysis of ROI-based mean T_1 values for the multi-slice in vivo mice abdomen experiments. Mean T_1 values of mice back-muscle, cortex, and pelvis regions for the TSE and CS-TSE acquisitions were compared by means of percentage mean T_1 differences. Each p value evaluated

by performing two-sided two sample t-test with unequal variances. * $p < 0.05$; ** $p < 0.01$; *** $p < 0.001$

						p value		
						#slice 2		#slice 8
			n	Mean T_1 (±SD) ms	Pct. mean T_1 diff. %	CS4-TSE2	TSE8	CS4-TSE2
Muscle	#slice 2	TSE2 (ref.)	8	1415 (±232)		0.2972	0.0000***	
		CS4-TSE2	8	1438 (±205)	1.63%		0.0000***	
		TSE8	8	1665 (±257)	17.67%			
	#slice 8	TSE2	8	1907 (±324)	34.77%			0.3939
		CS4-TSE2	8	1938 (±276)	36.96%			
Cortex	#slice 2	TSE2 (ref.)	8	1346 (±175)		0.2360	0.1008	
		CS4-TSE2	8	1287 (±157)	-4.38%		0.0108*	
		TSE8	8	1440 (±164)	6.98%			
	#slice 8	TSE2	8	1892 (±209)	40.56%			0.7675
		CS4-TSE2	8	1885 (±170)	40.04%			
Pelvis	#slice 2	TSE2 (ref.)	7	1779 (±322)		0.0643	0.0483*	
		CS4-TSE2	7	1703 (±225)	-4.27%		0.0044**	
		TSE8	8	1923 (±311)	8.09%			
	#slice 8	TSE2	7	2272 (±324)	27.71%			0.5943
		CS4-TSE2	6	2287 (±286)	28.56%			

5.4 Discussion

Adopting CS technique to the TSE acquisitions has been investigated for fast T_2 mapping [93], diffusion spectrum imaging [94], diffusion tensor imaging [95], cardiac MRI [96], and dynamic contrast-enhanced MRI [90]. In this study, we employed the CS technique to reduce the echo-train-length of the TSE methods especially for the multiple-TR T_1 measurement for preclinical scanner.

In the ex vivo results for the single-slice experiments, introducing a CS undersampling to the TSE pulse sequence (CS-TSE) enhanced the accuracy of the T_1 mapping in comparison to the conventional TSE method at the same total scan time. This can be explained through minimized T_2 relaxations of the CS-TSE against the TSE acquisition at the same total acceleration factors. The echo-trains of the conventional TSE acquisition heavily affected by the T_2 relaxations particularly in the high-frequency regions of the k-space. Thus, as long as the image degradation due to CS reconstruction is more tolerable than that from T_2 decaying, the CS-TSE is expected to provide better quality for the T_1 map than the TSE, which is in accordance with the simulation results for the multiple T_2 values. Therefore, investigating the advantages of the CS-TSE acquisition might be crucial for the application of dynamic T_1 quantification together with the injection of an exogenous MR contrast agent with the serious T_2 shortening, which might cause T_1 mapping errors.

It should be emphasized that, for the multi-slice T_1 mapping results of both ex vivo and in vivo experiments, the total number of RF excitations in a single TR period was depending on the number of slices × TF. In addition, the total scan times were in inverse proportion to TF × CS acceleration

factors. Therefore, for the two-slice T_1 measurements, the T_1 maps evaluated from the CS4-TSE2 provided a robust T_1 accuracy in respect of the standard T_1 values, whereas those from the TSE8 involved unacceptable T_1 overestimations. These T_1 errors largely caused by the inter-slice interferences due to the repeated excitation pulses which lock the recovery of the longitudinal magnetization in adjacent slices [87]. Thus, the blocked recovery of the longitudinal magnetization results in the overestimation of measured T_1 relaxation time in the multi-slice T_1 mapping with increasing TF. To solve these limitations of the TSE acquisition, employing the slice-gaps for the multi-slice acquisitions significantly successful to minimize the inter-slice interference induced the T_1 errors as shown in Figure 5.7. However, the T_1 overestimation caused by MT effect still incompletely compensated, and the slice-gap control may be restricted due to the typically small FOV size of rodent experiments.

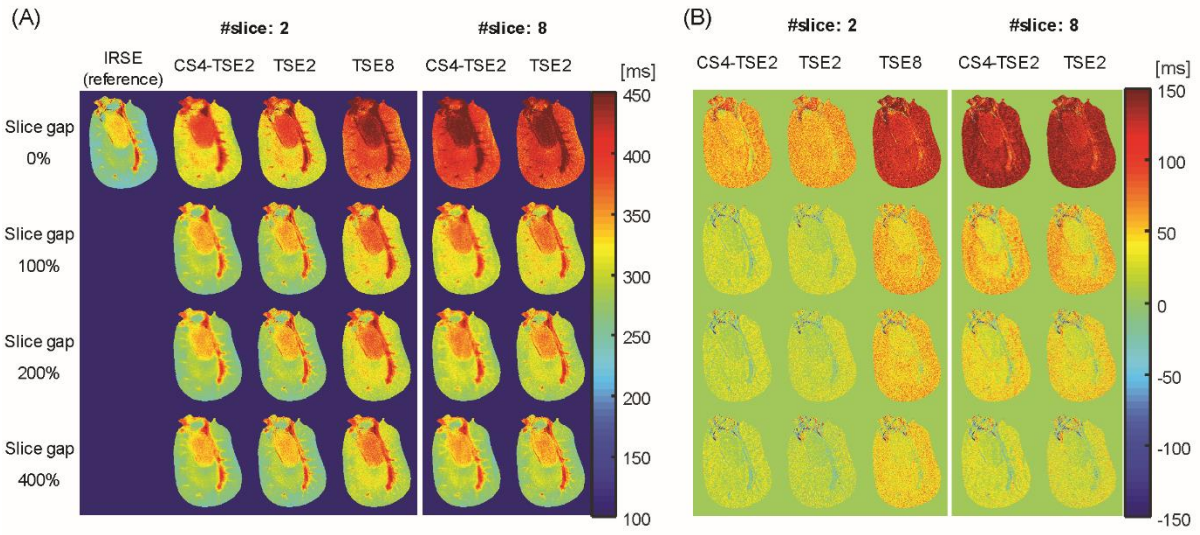

Figure 5.7 The effects of inter-slice interferences (crosstalk and MT) on the multi-slice T_1 mapping with TSE-based acquisitions. Multi-slice T_1 maps for the ex vivo rat kidney sample were obtained from gold standard IRSE, CS4-TSE2, TSE2, and TSE8 acquisitions with varying the slice-gaps (0, 100, 200, and 400%) (A). Corresponding T_1 differences were calculated in reference to the T_1 map from IRSE acquisition (B). The T_1 overestimations of both the TSE and CS-TSE reduced as increasing the slice-gaps, while the uncompensated T_1 overestimation still existed because of the MT effect.

For preclinical experiments, the advantages of employing spin-echo acquisition were significant over the reduction in the total scan time. Figure 5.8 illustrates the comparison results of the CS-TSE T_1 mapping with other gradient-echo based acquisitions, such as variable-flip-angle gradient-echo and inversion-recovery Look-Locker TrueFISP acquisitions, for the single-slice in vivo mouse abdomen

experiments. Briefly, spin-echo acquisition based both TSE and CS-TSE T_1 mapping methods shows better T_1 map qualities than the gradient-echo based T_1 mapping methods at 7 T.

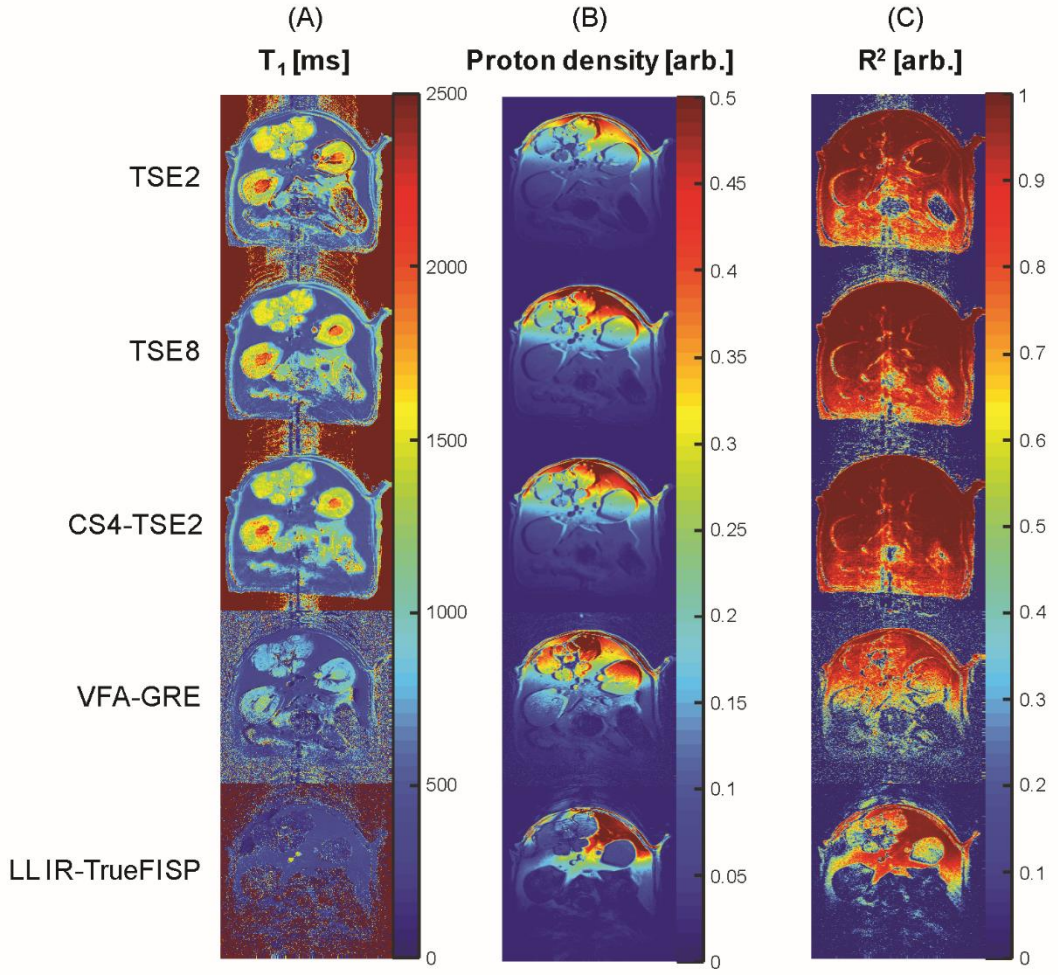

Figure 5.8 Comparison of different acquisitions for single-slice in vivo mouse abdomen T_1 mapping. The T_1 and proton density maps (A and B) derived from turbo spin-echo based acquisitions (TSE2, TSE8, and CS4-TSE2) provide stable map and fitting qualities (C) for the entire abdominal region. However, the gradient echo based variable flip angle and Look-Locker version of inversion recovery TrueFISP acquisitions suffer from T_1 accuracy and fitting quality issues in the region influenced by B_0 inhomogeneity at a 7 T preclinical system.

The limitations of the measurement of the MR T_1 relaxation time with the CS-TSE acquisition are discussed as follows. First, although the unwanted image blurring due to the T_2 relaxations in the high-frequency regions of the k-space is compensated by employing the sparse sampling with reduced an echo-train-length, image smoothing due to CS reconstruction were still observed for the resulting in vivo T_1 map from the CS-TSE method. Second, for the preclinical multi-slice T_1 measurements, the significant scan time reduction was accomplished with the CS-TSE over the conventional TSE

method (< 15-minute in this study), multiple-TRs of the TSE-based methods still hinder its clinical applications (typical requiring scan time under 5-minute for each acquisition). However, there is a margin to overcome these limitations for the clinical applications by utilizing improved image reconstruction algorithms combining with the parallel imaging technique, where a clinical MRI is usually obtained with larger FOV and acquisition matrix size, which enhance the acceleration efficiency of the sparse sampling techniques. Therefore, improved CS-TSE T_1 mapping in a clinical system may further minimize the unwanted image blurring at an acceptable total scan time, which could be beneficial to the anatomical region with inevitable several B_0 inhomogeneities and low SNR due to short T_2 relaxations.

In conclusion, the advantages of the multi-slice CS-TSE T_1 mapping over the conventional TSE and gradient-echo based fast acquisition were explored. By the aid of minimized echo-train-length of the CS-TSE, a robust multi-slice T_1 mapping for the acceptable scan times under 15-minuit was achieved with minimized in inter-slice interferences, influence from the B_0 inhomogeneity, and T_2 relaxation induced image blurring for multi-slice coverage, which are all critical for the in absolute T_1 measurement at high magnetic field (> 7 T) preclinical applications.

6. References

1. Griffiths HJ. The Evaluation of Osteoporosis: Dual Energy X-ray Absorptiometry in Clinical Practice. Radiology 1994;192:332-332.
2. Kanis JA. Diagnosis of osteoporosis and assessment of fracture risk. Lancet 2002;359:1929-36.
3. Jain RK, Vokes T. Dual-energy X-ray Absorptiometry. J Clin Densitom 2017;20:291-303.
4. Organization WH. Assessment of fracture risk and its application to screening for postmenopausal osteoporosis: report of a WHO study group [meeting held in Rome from 22 to 25 June 1992]. 1994.
5. NIH Consensus Development Panel on Osteoporosis Prevention, Diagnosis, and Therapy, March 7-29, 2000: highlights of the conference. South Med J 2001;94:569-73.
6. Wehrli FW. Structural and functional assessment of trabecular and cortical bone by micro magnetic resonance imaging. J Magn Reson Imaging 2007;25:390-409.
7. Damilakis J, Adams JE, Guglielmi G, Link TM. Radiation exposure in X-ray-based imaging techniques used in osteoporosis. Eur Radiol 2010;20:2707-2714.
8. Gervaise A, Teixeira P, Villani N, Lecocq S, Louis M, Blum A. CT dose optimisation and reduction in osteoarticular disease. Diagn Interv Imaging 2013;94:371-88.
9. Chang G, Boone S, Martel D, Rajapakse CS, Hallyburton RS, Valko M, Honig S, Regatte RR. MRI assessment of bone structure and microarchitecture. J Magn Reson Imaging 2017;46:323-337.
10. Gomberg BR, Wehrli FW, Vasilic B, Weening RH, Saha PK, Song HK, Wright AC. Reproducibility and error sources of mu-MRI-based trabecular bone structural parameters of the distal radius and tibia. Bone 2004;35:266-276.
11. Kim N, Lee JG, Song Y, Kim HJ, J SY, Cho G. Evaluation of MRI resolution affecting trabecular bone parameters: determination of acceptable resolution. Magn Reson Med 2012;67:218-25.
12. Bauer JS, Sidorenko I, Mueller D, Baum T, Issever AS, Eckstein F, Rummeny EJ, Link TM, Raeth CW. Prediction of bone strength by muCT and MDCT-based finite-element-models: how much spatial resolution is needed? Eur J Radiol 2014;83:e36-42.
13. Lowitz T, Museyko O, Bousson V, Kalender WA, Laredo JD, Engelke K. A Digital Model to Simulate Effects of Bone Architecture Variations on Texture at Spatial Resolutions of CT, HR-pQCT, and muCT Scanners. J Med Eng 2014;2014:946574.
14. Ford JC, Wehrli FW. In vivo quantitative characterization of trabecular bone by NMR interferometry and localized proton spectroscopy. Magn Reson Med 1991;17:543-51.

15. Majumdar S, Thomasson D, Shimakawa A, Genant HK. Quantitation of the Susceptibility Difference between Trabecular Bone and Bone-Marrow - Experimental Studies. Magn Reson Med 1991;22:111-127.
16. Wehrli F, Ford J, Attie M, Kressel H, Kaplan F. Trabecular structure: preliminary application of MR interferometry. Radiology 1991;179:615-621.
17. Chung H, Wehrli F, Williams J, Kugelmass S. Relationship between NMR transverse relaxation, trabecular bone architecture, and strength. Proceedings of the National Academy of Sciences 1993;90:10250-10254.
18. Selby K, Majumdar S, Newitt DC, Genant HK. Investigation of MR decay rates in microphantom models of trabecular bone. J Magn Reson Imaging 1996;6:549-59.
19. Link TM, Majumdar S, Augat P, Lin JC, Newitt D, Lane NE, Genant HK. Proximal femur: assessment for osteoporosis with T2* decay characteristics at MR imaging. Radiology 1998;209:531-536.
20. Hwang SN, Wehrli FW. Experimental evaluation of a surface charge method for computing the induced magnetic field in trabecular bone. J Magn Reson 1999;139:35-45.
21. Capuani S, Curzi F, Alessandri FM, Maraviglia B, Bifone A. Characterization of trabecular bone by dipolar demagnetizing field MRI. Magn Reson Med 2001;46:683-9.
22. Lammentausta E, Silvast T, Närväinen J, Jurvelin J, Nieminen M, Gröhn O. T2, Carr–Purcell T2 and T1ρ of fat and water as surrogate markers of trabecular bone structure. Phys Med Biol 2008;53:543.
23. Sigmund EE, Cho H, Song YQ. High-resolution MRI of internal field diffusion-weighting in trabecular bone. NMR Biomed 2009;22:436-48.
24. De Santis S, Rebuzzi M, Di Pietro G, Fasano F, Maraviglia B, Capuani S. In vitro and in vivo MR evaluation of internal gradient to assess trabecular bone density. Phys Med Biol 2010;55:5767-85.
25. Rebuzzi M, Vinicola V, Taggi F, Sabatini U, Wehrli FW, Capuani S. Potential diagnostic role of the MRI-derived internal magnetic field gradient in calcaneus cancellous bone for evaluating postmenopausal osteoporosis at 3T. Bone 2013;57:155-63.
26. Sprinkhuizen SM, Ackerman JL, Song YQ. Influence of bone marrow composition on measurements of trabecular microstructure using decay due to diffusion in the internal field MRI: Simulations and clinical studies. Magn Reson Med 2013.
27. Wurnig MC, Calcagni M, Kenkel D, Vich M, Weiger M, Andreisek G, Wehrli FW, Boss A. Characterization of trabecular bone density with ultra-short echo-time MRI at 1.5, 3.0 and 7.0 T–comparison with micro-computed tomography. NMR Biomed 2014;27:1159-1166.

28. Young IR, Cox IJ, Bryant DJ, Bydder GM. The Benefits of Increasing Spatial-Resolution as a Means of Reducing Artifacts Due to Field Inhomogeneities. Magn Reson Imaging 1988;6:585-590.
29. Frahm J, Merboldt KD, Hanicke W. Functional Mri of Human Brain Activation at High Spatial-Resolution. Magn Reson Med 1993;29:139-144.
30. Regatte RR, Schweitzer ME. Ultra-high-field MRI of the musculoskeletal system at 7.0 T. Journal of Magnetic Resonance Imaging 2007;25:262-269.
31. Khosla S, Riggs BL, Atkinson EJ, Oberg AL, McDaniel LJ, Holets M, Peterson JM, Melton LJ. Effects of Sex and Age on Bone Microstructure at the Ultradistal Radius: A Population-Based Noninvasive In Vivo Assessment. Journal of bone and mineral research : the official journal of the American Society for Bone and Mineral Research 2006;21:124-131.
32. Pathak AP, Ward BD, Schmainda KM. A novel technique for modeling susceptibility-based contrast mechanisms for arbitrary microvascular geometries: the finite perturber method. Neuroimage 2008;40:1130-43.
33. Han SH, Cho JH, Jung HS, Suh JY, Kim JK, Kim YR, Cho G, Cho H. Robust MR assessment of cerebral blood volume and mean vessel size using SPION-enhanced ultrashort echo acquisition. Neuroimage 2015;112:382-9.
34. Jung H, Jin S, Cho J, Han S, Lee D, Cho H. UTE–ΔR2–ΔR2* combined MR whole-brain angiogram using dual-contrast superparamagnetic iron oxide nanoparticles. NMR Biomed 2016;29:690-701.
35. Lideed D. CRC Handbook of Chemistry and Physics, Internet Version 2005. Boca Raton, FL: CRC Press; 2005.
36. Folch J, Lees M, Sloane-Stanley G. A simple method for the isolation and purification of total lipids from animal tissues. J biol Chem 1957;226:497-509.
37. Otsu N. A threshold selection method from gray-level histograms. IEEE Transactions on Systems, Man, and Cybernetics 1979;9:62-66.
38. Dougherty R, Kunzelmann K-H. Computing local thickness of 3D structures with ImageJ. Microscopy and Microanalysis 2007;13:1678.
39. Hildebrand T, Rüegsegger P. A new method for the model-independent assessment of thickness in three-dimensional images. J Microsc 1997;185:67-75.
40. Doube M, Klosowski MM, Arganda-Carreras I, Cordelieres FP, Dougherty RP, Jackson JS, Schmid B, Hutchinson JR, Shefelbine SJ. BoneJ: Free and extensible bone image analysis in ImageJ. Bone 2010;47:1076-9.
41. Blumenkrantz G, Lindsey CT, Dunn TC, Jin H, Ries MD, Link TM, Steinbach LS, Majumdar S. A pilot, two-year longitudinal study of the interrelationship between trabecular bone and articular cartilage in the osteoarthritic knee. Osteoarthritis Cartilage 2004;12:997-1005.

42. Lindsey CT, Narasimhan A, Adolfo JM, Jin H, Steinbach LS, Link T, Ries M, Majumdar S. Magnetic resonance evaluation of the interrelationship between articular cartilage and trabecular bone of the osteoarthritic knee. Osteoarthritis Cartilage 2004;12:86-96.
43. Bolbos RI, Zuo J, Banerjee S, Link TM, Ma CB, Li X, Majumdar S. Relationship between trabecular bone structure and articular cartilage morphology and relaxation times in early OA of the knee joint using parallel MRI at 3T. Osteoarthritis Cartilage 2008;16:1150-1159.
44. Chang G, Wang L, Liang G, Babb JS, Wiggins GC, Saha PK, Regatte RR. Quantitative assessment of trabecular bone micro-architecture of the wrist via 7 Tesla MRI: preliminary results. MAGMA 2011;24:191-9.
45. Capuani S, Rebuzzi M, Fasano F, Hagberg G, Di Mario M, Vinicola10 V, Maraviglia B. T2*-relaxometry and 1H-MRS at 3T applied to healthy and osteoporotic subjects: preliminary data supporting a new procedure to evaluate bone fracture risk. Young 2008;16:18.
46. Sprinkhuizen SM, Ackerman JL, Song YQ. Influence of Bone Marrow Composition on Measurements of Trabecular Microstructure Using Decay Due to Diffusion in the Internal Field MRI: Simulations and Clinical Studies. Magn Reson Med 2014;72:1499-1508.
47. Boxerman JL, Hamberg LM, Rosen BR, Weisskoff RM. Mr Contrast Due to Intravascular Magnetic-Susceptibility Perturbations. Magnetic Resonance in Medicine 1995;34:555-566.
48. Dennie J, Mandeville JB, Boxerman JL, Packard SD, Rosen BR, Weisskoff RM. NMR imaging of changes in vascular morphology due to tumor angiogenesis. Magnetic Resonance in Medicine 1998;40:793-799.
49. Tropres I, Grimault S, Vaeth A, Grillon E, Julien C, Payen JF, Lamalle L, Decorps M. Vessel size imaging. Magn Reson Med 2001;45:397-408.
50. Kiselev VG, Posse S. Analytical model of susceptibility-induced MR signal dephasing: effect of diffusion in a microvascular network. Magn Reson Med 1999;41:499-509.
51. Kim SG, Harel N, Jin T, Kim T, Lee P, Zhao F. Cerebral blood volume MRI with intravascular superparamagnetic iron oxide nanoparticles. NMR Biomed 2013;26:949-62.
52. Rivera-Rivera LA, Schubert T, Knobloch G, Turski PA, Wieben O, Reeder SB, Johnson KM. Comparison of ferumoxytol-based cerebral blood volume estimates using quantitative R1 and relaxometry. Magnetic resonance in medicine 2018;79:3072-3081.
53. Song Y-Q. Determining pore sizes using an internal magnetic field. Elsevier; 2000.
54. Cho HJ, Sigmund EE, Song YQ. Magnetic Resonance Characterization of Porous Media Using Diffusion through Internal Magnetic Fields. Materials 2012;5:590-616.
55. Chung JR, Sung C, Mayerich D, Kwon J, Miller DE, Huffman T, Abbott LC, Keyser J, Choe Y. Multiscale exploration of mouse brain microstructures using the knife-edge scanning microscope brain atlas. Frontiers in neuroinformatics 2011;5:29.

56. Tropres I, Pannetier N, Grand S, Lemasson B, Moisan A, Peoc'h M, Remy C, Barbier EL. Imaging the Microvessel Caliber and Density: Principles and Applications of Microvascular MRI. Magnetic Resonance in Medicine 2015;73:325-341.
57. Song YQ. Using internal magnetic fields to obtain pore size distributions of porous media. Concepts in Magnetic Resonance Part A: An Educational Journal 2003;18:97-110.
58. Schlageter KE, Molnar P, Lapin GD, Groothuis DR. Microvessel organization and structure in experimental brain tumors: microvessel populations with distinctive structural and functional properties. Microvasc Res 1999;58:312-28.
59. Mayerich D, Abbott L, McCormick B. Knife-edge scanning microscopy for imaging and reconstruction of three-dimensional anatomical structures of the mouse brain. J Microsc 2008;231:134-43.
60. Mayerich D, Kwon J, Sung C, Abbott L, Keyser J, Choe Y. Fast macro-scale transmission imaging of microvascular networks using KESM. Biomedical Optics Express 2011;2:2888-2896.
61. Bakker R, Tiesinga P, Kotter R. The Scalable Brain Atlas: Instant Web-Based Access to Public Brain Atlases and Related Content. Neuroinformatics 2015;13:353-66.
62. Duvernoy H, Delon S, Vannson J. The vascularization of the human cerebellar cortex. Brain research bulletin 1983;11:419-480.
63. Lauwers F, Cassot F, Lauwers-Cances V, Puwanarajah P, Duvernoy H, Morphometry of the human cerebral cortex microcirculation: General characteristics and space-related profiles. NeuroImage 2008;39:936-948.
64. Lustig M, Donoho D, Pauly JM. Sparse MRI: The application of compressed sensing for rapid MR imaging. Magnetic Resonance in Medicine: An Official Journal of the International Society for Magnetic Resonance in Medicine 2007;58:1182-1195.
65. Bottomley P, Hardy C, Argersinger R, Allen-Moore G. A review of 1H nuclear magnetic resonance relaxation in pathology: Are T1 and T2 diagnostic? Med Phys 1987;14:1-37.
66. Leach M, Brindle K, Evelhoch J, Griffiths J, Horsman M, Jackson A, Jayson G, Judson I, Knopp M, Maxwell R, McIntyre D, Padhani A, Price P, Rathbone R, Rustin G, Tofts P, Tozer G, Vennart W, Waterton J, Williams S, Workmanw P. The assessment of antiangiogenic and antivascular therapies in early-stage clinical trials using magnetic resonance imaging: Issues and recommendations. Brit J Cancer 2005;92:1599-1610.
67. Tofts P. Quantitative MRI of the brain: Measuring changes caused by disease: John Wiley & Sons; 2005.
68. Carr HY, Purcell EM. Effects of diffusion on free precession in nuclear magnetic resonance experiments. Phys Rev 1954;94(3):630-638.

69. McDonald GG, Leigh JS. A new method for measuring longitudinal relaxation times. J Magn Reson 1973;9:358-362.
70. Look DC, Locker DR. Time saving in measurement of NMR and EPR relaxation times. Rev Sci Instrum 1970;41:250-251.
71. Messroghli DR, Radjenovic A, Kozerke S, Higgins DM, Sivananthan MU, Ridgway JP. Modified Look-Locker inversion recovery (MOLLI) for high-resolution T1 mapping of the heart. Magn Reson Med 2004;52:141-146.
72. Piechnik SK, Ferreira VM, Dall'Armellina E, Cochlin LE, Greiser A, Neubauer S, Robson MD. Shortened Modified Look-Locker Inversion recovery (ShMOLLI) for clinical myocardial T1-mapping at 1.5 and 3 T within a 9 heartbeat breathhold. J Cardiovasc Magn Reson 2010;12:69.
73. Fram EK, Herfkens RJ, Johnson GA, Glover GH, Karis JP, Shimakawa A, Perkins TG, Pelc NJ. Rapid calculation of T1 using variable flip angle gradient refocused imaging. Magn Reson Imaging 1987;5:201-208.
74. Brookes JA, Redpath TW, Gilbert FJ, Murray AD, Staff RT. Accuracy of T1 measurement in dynamic contrast-enhanced breast MRI using two-and three-dimensional variable flip angle fast low-angle shot. J Magn Reson Imaging 1999;9:163-171.
75. Cheng HLM, Wright GA. Rapid high-resolution T1 mapping by variable flip angles: Accurate and precise measurements in the presence of radiofrequency field inhomogeneity. Magn Reson Med 2006;55:566-574.
76. Stikov N, Boudreau M, Levesque IR, Tardif CL, Barral JK, Pike GB. On the accuracy of T1 mapping: searching for common ground. Magn Reson Med 2015;73:514-522.
77. Hennig J, Nauerth A, Friedburg H. RARE imaging: A fast imaging method for clinical MR. Magn Reson Med 1986;3:823-833.
78. Constable R, Anderson A, Zhong J, Gore J. Factors influencing contrast in fast spin-echo MR imaging. Magn Reson Imaging 1992;10(4):497-511.
79. Jung H, Sung K, Nayak KS, Kim EY, Ye JC. k-t FOCUSS: A general compressed sensing framework for high resolution dynamic MRI. Magn Reson Med 2009;61:103-116.
80. Han S, Paulsen JL, Zhu G, Song Y, Chun S, Cho G, Ackerstaff E, Koutcher JA, Cho H. Temporal/spatial resolution improvement of in vivo DCE-MRI with compressed sensing-optimized FLASH. Magn Reson Imaging 2012;30:741-752.
81. Doneva M, Börnert P, Eggers H, Stehning C, Sénégas J, Mertins A. Compressed sensing reconstruction for magnetic resonance parameter mapping. Magn Reson Med 2010;64:1114-1120.

82. Huang C, Graff CG, Clarkson EW, Bilgin A, Altbach MI. T2 mapping from highly undersampled data by reconstruction of principal component coefficient maps using compressed sensing. Magn Reson Med 2012;67:1355-1366.
83. Li W, Griswold M, Yu X. Fast cardiac T1 mapping in mice using a model-based compressed sensing method. Magn Reson Med 2012;68:1127-1134.
84. Wu B, Li W, Guidon A, Liu C. Whole brain susceptibility mapping using compressed sensing. Magn Reson Med 2012;67:137-147.
85. Velikina JV, Alexander AL, Samsonov A. Accelerating MR parameter mapping using sparsity-promoting regularization in parametric dimension. Magn Reson Med 2013;70:1263-1273.
86. Hendrick RE, Raff U. Image Contrast and Noise. DD Stark, WG Bradley (Eds), Magnetic Resonance Imaging (2nd Edition), Mosby-Year Book, St Louis, Missouri 1992:109-144.
87. Yamada S, Matsuzawa T, Yamada K, Yoshioka S, Ono S, Hishinuma T. A modified signal intensity equation of carr-purcell-meiboom-gill pulse sequence for MR imaging. Tohoku J Exp Med 1989;158(3):203-209.
88. Efraimidis PS, Spirakis PG. Weighted random sampling with a reservoir. Inform Process Lett 2006;97(5):181-185.
89. Lawrence I, Lin K. A concordance correlation coefficient to evaluate reproducibility. Biometrics 1989:255-268.
90. Han S, Cho H. Temporal resolution improvement of calibration-free dynamic contrast-enhanced MRI with compressed sensing optimized turbo spin echo: The effects of replacing turbo factor with compressed sensing accelerations. J Magn Reson Imaging 2015.
91. Van Den Berg E, Friedlander MP. Probing the Pareto frontier for basis pursuit solutions. SIAM J Sci Comput 2008;31:890-912.
92. Donoho DL, Stodden VC, Tsaig Y. About sparselab. 2007.
93. Feng L, Otazo R, Jung H, Jensen JH, Ye JC, Sodickson DK, Kim D. Accelerated cardiac T2 mapping using breath-hold multiecho fast spin-echo pulse sequence with k-t FOCUSS. Magn Reson Med 2011;65:1661-1669.
94. Teh I, Lohezic M, Aksentijevic D, Schneider J. Accelerated fast spin echo diffusion spectrum imaging in the mouse heart ex-vivo. J Cardiovasc Magn Reson 2013;15:W6.
95. McClymont D, Teh I, Whittington HJ, Grau V, Schneider JE. Prospective acceleration of diffusion tensor imaging with compressed sensing using adaptive dictionaries. Magn Reson Med 2015.
96. Boesen ME, Neto M, Souto LA, Pulwicki A, Yerly J, Lebel RM, Frayne R. Fast spin echo imaging of carotid artery dynamics. Magn Reson Med 2014;74:1103-1109.

7. Acknowledgements

I deeply appreciate my adviser, Professor Hyungjoon Cho, for his unconditional support. He has always treated me like a real family. Working with him is one of the best things in my life. And I sincerely thank my lab mates, Hanso, Hoesu, Myungsoo, Seokha, Hansol, Minjung, and Hwapyeong-Soonji, who spent most of my graduate school days and nights and care each other like brothers and sisters. I will always keep the memories through my life.